

# Self-consistent clustering analysis: an efficient multi-scale scheme for inelastic heterogeneous materials

Zeliang Liu<sup>a</sup>, M.A. Bessa<sup>b</sup>, Wing Kam Liu<sup>b,\*</sup>

<sup>a</sup>*Theoretical and Applied Mechanics, Northwestern University, Evanston, IL 60208, USA*

<sup>b</sup>*Department of Mechanical Engineering, Northwestern University, Evanston, IL 60208, USA*

---

## Abstract

The discovery of efficient and accurate descriptions for the macroscopic behavior of materials with complex microstructure is an outstanding challenge in mechanics of materials. A mechanistic, data-driven, two-scale approach is developed for predicting the behavior of general heterogeneous materials under irreversible processes such as inelastic deformation. The proposed approach includes two major innovations: 1) the use of a data compression algorithm, k-means clustering, during the offline stage of the method to homogenize the local features of the material microstructure into a group of clusters; and 2) a new method called self-consistent clustering analysis used in the online stage that is valid for any local plasticity laws of each material phase without the need for additional calibration. A particularly important feature of the proposed approach is that the offline stage only uses the linear elastic properties of each material phase, making it efficient. This work is believed to open new avenues in parameter-free multi-scale modeling of complex materials, and perhaps in other fields that require homogenization of irreversible processes.

*Keywords:* multi-scale, reduced order model, plasticity, data compression, k-means clustering, self-consistent method

---

## 1. Introduction

Materials are hierarchical in nature, involving an inter-play between simple small-scale constituents that together form elaborate compounds that can span multiple time- and length-scales. This multi-scale nature of heterogeneous materials poses a continuing challenge in computational modeling of macroscopic structures. Ideally, efficient and accurate predictions of the macroscopic behavior of heterogeneous materials should be uniquely obtained from the constitutive behavior of each separate constituent (material phase) and from the information about the material microstructure.

Traditional phenomenological constitutive relations [1, 2, 3] characterize the average behaviors of the material, i.e the contributions from all the material phases are not accounted for as an individual interaction of separate constituents. These laws regard materials as “black boxes,” implying the need for burdensome experimental characterization and tedious calibration. In addition, they are problem-dependent and tend to fail when capturing highly localized microstructure-induced nonlinear material behaviors, such as plasticity, damage and fatigue.

Concurrent multiscale methods [4, 5, 6, 7, 8, 9, 10, 11] avoid this calibration process by directly establishing the connection between the microstructure and the macro-response of materials. These concurrent methods link to *every* macroscopic point of a structure a high-fidelity simulation of a Representative Unit Cell (RUC) [12, 13] of the microstructure. Since each RUC is already associated to a large computational cost, the total computational cost of this approach is tremendous.

---

\*Corresponding author

*Email address:* w-liu@northwestern.edu (Wing Kam Liu)

19 A myriad of methods have been developed with the goal of finding an appropriate balance between cost  
20 and accuracy; these are generally referred as reduced order models. Analytical micromechanical methods  
21 [14, 15, 16, 17], the Voronoi cell finite element method [18], fast Fourier transforms [19], spectral methods  
22 [20], the generalized method of cells [21], the transformation field analysis (TFA) [22], the nonuniform trans-  
23 formation field analysis (NTFA) [23, 24], the principal component analysis [25, 26, 27] or proper orthogonal  
24 decomposition<sup>1</sup> (POD) [28, 29, 30, 31], and the proper generalized decomposition (PGD) [32, 33, 34, 35, 36]  
25 are some of the most successful methods of this kind.

26 Analytical micromechanical methods [14, 15, 16, 17] are very efficient because they describe the hetero-  
27 geneous material by several microstructural descriptors, rather than considering the whole representative  
28 unit cell explicitly. However, they are based on mean-field assumptions and linear superposition. This limits  
29 their applicability when complex microstructure and localized nonlinear material behavior such as plasticity  
30 are present.

31 POD uses linear combinations of all input variables to define the principal components (modes) to make  
32 the predictions for general load cases. This is a fundamental issue when describing nonlinear irreversible  
33 plastic processes that is only mitigated by using many snapshots in the offline stage which increases the  
34 computational cost of the online stage to unreasonable values [29, 37].

35 The NTFA introduced by Michel and Suquet [23] and further explored by Oskay and Fish [38] among  
36 others [39, 40], approaches the problem differently with the aim of drastically reducing computational cost  
37 [39]. The idea behind NTFA is to leverage the capabilities of analytical micromechanical methods to define  
38 a set of reduced variables (e.g. plastic strain fields and internal variables of the local constitutive laws)  
39 that are then subjected to “evolution equations” [23, 41]. Consequently, the computational cost of NTFA  
40 is low but the inclusion of empirical laws that require further calibration is a limitation. Furthermore, the  
41 representative unit cells need to be subjected to irreversible deformation to obtain the plastic modes (as in  
42 POD) which leads to an extensive exploration of the deformation space at the offline stage.

43 In this article a new approach is proposed where the above-mentioned limitations are addressed simul-  
44 taneously by meeting three fundamental goals: 1) avoiding to have an extensive exploratory offline stage  
45 (as in NTFA and especially POD), by limiting this stage to the characterization of the *elastic behavior*  
46 of the representative unit cell; 2) eliminating the need to find reduced macro-constitutive equations (as in  
47 NTFA), i.e. only using the local constitutive equations of each phase present in the representative unit cell  
48 without calibration of additional laws; and 3) achieving a reduction in computational time of several orders  
49 of magnitude without significantly compromising accuracy.

50 In order to achieve these goals *two fundamental contributions* are introduced in Section 2: a new analysis  
51 method applicable to any reduced RUC; and a procedure based on a data compression algorithm to obtain  
52 any reduced RUC. Section 3 shows the results and discusses the accuracy and efficiency of the methodology.  
53 Concluding remarks are provided in Section 4.

## 54 2. Methodology

55 The starting point is a high-fidelity Representative Unit Cell (RUC) of the material, i.e. a representative  
56 domain of the microstructure of a material. This high-fidelity RUC can be analyzed by different methods, e.g.  
57 finite element or meshfree methods, such that accurate predictions of the material’s mechanical behavior are  
58 achieved. However, the computational cost associated to these RUCs is usually significantly large because  
59 they involve a very fine numerical discretization to capture the microstructural shapes of the material and  
60 its detailed mechanical behavior.

61 With the aim of lowering the computational expense one may consider to decompose the high-fidelity  
62 RUC into a group of large subdomains, obtaining a reduced RUC – Figure 1. These subdomains are  
63 designated as **material clusters** henceforth. However, if one uses the same analysis method considered  
64 for the high-fidelity RUC, the resolution for the analysis is degraded and the accuracy of the predictions  
65 decreases. For example, if using the finite element method the larger subdomains (material clusters) would

---

<sup>1</sup>The mechanics community refers to principal component analysis as proper orthogonal decomposition (POD).

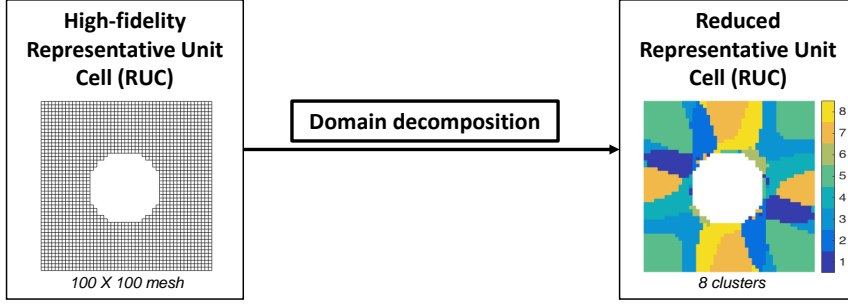


Figure 1: Illustration of arbitrary domain decomposition for a high-fidelity RUC transforming it into a reduced RUC with just 8 subdomains (clusters).

66 have to correspond to larger finite elements, introducing limitations in the shape of these clusters and the  
 67 accuracy of the solution.

68 This poses an interesting question: for large and irregular material clusters, what is the appro-  
 69 priate analysis method that maintains good accuracy for the predictions of the reduced RUC?

70 In order to answer this question, assume an arbitrary domain decomposition of the RUC. The procedure  
 71 used to determine these material clusters will be introduced later in Section 2.2.1. In addition, assume  
 72 that *every local variable  $\beta(\mathbf{x})$  within each material cluster is uniform*. This is equivalent to considering a  
 73 piecewise uniform approximation to the local variables of interest in the RUC<sup>2</sup>:

$$\beta(\mathbf{x}) = \sum_{I=1}^k \beta^I \chi^I(\mathbf{x}), \quad (1)$$

74 where  $\beta^I$  is the homogeneous variable in the  $I$ -th material cluster and  $\chi^I(\mathbf{x})$  is the characteristic function  
 75 in the domain of the  $I$ -th material cluster  $\Omega^I$ , defined as

$$\chi^I(\mathbf{x}) = \begin{cases} 1 & \text{if } x \in \Omega^I \\ 0 & \text{otherwise} \end{cases} \quad (2)$$

76 from which the following cluster averaging relationship can be written,

$$\int_{\Omega} \chi^I(\mathbf{x}) [\bullet] d\mathbf{x} \equiv \int_{\Omega^I} [\bullet] d\mathbf{x} \quad (3)$$

77 where  $[\bullet]$  signifies any quantity of interest to be averaged in the cluster domain  $\Omega^I$ .

78 Under these assumptions, a system of equations can be derived by successively homogenizing each mate-  
 79 rial cluster via the Lippmann-Schwinger equation. The procedure is applicable to any domain decomposition  
 80 considered and is presented next.

### 81 2.1. Lippmann-Schwinger homogenization for multiple clusters

82 Generally, the equilibrium condition without body force in a material domain  $\Omega$  can be written as

$$\frac{\partial \sigma_{ij}(\mathbf{x})}{\partial x_i} = 0 \quad \text{in } \Omega. \quad (4)$$

<sup>2</sup>For example, if the variable of interest is local strain:  $\beta(\mathbf{x}) \equiv \varepsilon(\mathbf{x})$

83 By introducing a homogeneous isotropic linear elastic reference material with stiffness  $\mathbf{C}^0$ , the real stress in  
 84 the heterogeneous material can be divided into two parts,

$$\boldsymbol{\sigma}(\mathbf{x}) = \mathbf{C}^0 : \boldsymbol{\varepsilon}(\mathbf{x}) + \mathbf{p}(\mathbf{x}), \quad (5)$$

85 where  $\mathbf{p}(\mathbf{x})$  is the so-called polarization stress, which denotes the difference between the real stress and the  
 86 stress in the reference material under the same strain. By substituting equation (5) into (4), we obtain

$$C_{ijkl}^0 \frac{\partial \varepsilon_{kl}(\mathbf{x})}{\partial x_i} = - \frac{\partial p_{ij}(\mathbf{x})}{\partial x_i} \quad \text{in } \Omega. \quad (6)$$

87 With the help of the Green's function  $\Phi^0(\mathbf{x}, \mathbf{x}')$  which represents the strain at  $\mathbf{x}$  contributed by a concentrated  
 88 external stress at  $\mathbf{x}'$  in a homogeneous reference material, the original equilibrium condition can be rewritten  
 89 in an integral form if we regard the polarization stress as an external stress on the reference material [15, 42],  
 90

$$\boldsymbol{\varepsilon}(\mathbf{x}) + \int_{\Omega} \Phi^0(\mathbf{x}, \mathbf{x}') : \mathbf{p}(\mathbf{x}') d\mathbf{x}' - \boldsymbol{\varepsilon}^0 = 0, \quad (7)$$

91 where  $\boldsymbol{\varepsilon}^0$  is the far-field strain, which is homogeneous in the reference material and controls the evolution of  
 92 the strain  $\boldsymbol{\varepsilon}(\mathbf{x})$ . By substituting equation (5) into (7), we obtain the integral equation in terms of the local  
 93 strain  $\boldsymbol{\varepsilon}(\mathbf{x})$ ,

$$\boldsymbol{\varepsilon}(\mathbf{x}) + \int_{\Omega} \Phi^0(\mathbf{x}, \mathbf{x}') : [\boldsymbol{\sigma}(\mathbf{x}') - \mathbf{C}^0 : \boldsymbol{\varepsilon}(\mathbf{x}')] d\mathbf{x}' - \boldsymbol{\varepsilon}^0 = 0. \quad (8)$$

94 In order to solve  $\boldsymbol{\varepsilon}(\mathbf{x})$  in the integral equation (8), constraints are needed from the macroscopic boundary  
 95 conditions. In specific, if a macro-strain constraint is used:

$$\frac{1}{|\Omega|} \int_{\Omega} \boldsymbol{\varepsilon}(\mathbf{x}) d\mathbf{x} = \bar{\boldsymbol{\varepsilon}}, \quad (9)$$

96 or if a macro-stress constraint is considered:

$$\frac{1}{|\Omega|} \int_{\Omega} \boldsymbol{\sigma}(\mathbf{x}) d\mathbf{x} = \bar{\boldsymbol{\sigma}}. \quad (10)$$

97 Similarly, we can also define mixed constraints. For example, the constraints under uniaxial tension loading  
 98 are

$$\frac{1}{|\Omega|} \int_{\Omega} \varepsilon_{11}(\mathbf{x}) d\mathbf{x} = \bar{\varepsilon}_{11} \quad \text{if } i = j = 1; \quad \text{otherwise, } \frac{1}{|\Omega|} \int_{\Omega} \sigma_{ij}(\mathbf{x}) d\mathbf{x} = \bar{\sigma}_{ij} = 0. \quad (11)$$

99 For convenience, equation (8) can be written in incremental form:

$$\Delta \boldsymbol{\varepsilon}(\mathbf{x}) + \int_{\Omega} \Phi^0(\mathbf{x}, \mathbf{x}') : [\Delta \boldsymbol{\sigma}(\mathbf{x}') - \mathbf{C}^0 : \Delta \boldsymbol{\varepsilon}(\mathbf{x}')] d\mathbf{x}' - \Delta \boldsymbol{\varepsilon}^0 = 0, \quad (12)$$

100 Integral equation (8) or (12) are also known as Lippmann-Schwinger equation, and solving such an  
 101 integral equation for every point would be very time-consuming and even slower than the actual simulation  
 102 of the high-fidelity RUC using finite element analysis, for example. However, recall that the high-fidelity  
 103 RUC was decomposed into finite material clusters to form a reduced RUC (see Figure 2). With this in mind,  
 104 the Lippmann-Schwinger equation is averaged for **each** cluster:

$$\frac{1}{c^I |\Omega|} \int_{\Omega} \chi^I(\mathbf{x}) \Delta \boldsymbol{\varepsilon}(\mathbf{x}) d\mathbf{x} + \frac{1}{c^I |\Omega|} \int_{\Omega} \int_{\Omega} \chi^I(\mathbf{x}) \Phi^0(\mathbf{x}, \mathbf{x}') : [\Delta \boldsymbol{\sigma}(\mathbf{x}') - \mathbf{C}^0 : \Delta \boldsymbol{\varepsilon}(\mathbf{x}')] d\mathbf{x}' d\mathbf{x} - \Delta \boldsymbol{\varepsilon}^0 = 0, \quad (13)$$

105 where this equation follows directly from averaging equation (12) within the  $I$ -th cluster, and where the first  
 106 term corresponds to  $\Delta \boldsymbol{\varepsilon}^I$ . Moreover, recalling the piecewise uniform assumption of all the local variables,  
 107 equation (1),

$$\Delta \boldsymbol{\varepsilon}(\mathbf{x}) = \sum_{J=1}^k \chi^J(\mathbf{x}) \Delta \boldsymbol{\varepsilon}^J, \quad \Delta \boldsymbol{\sigma}(\mathbf{x}) = \sum_{J=1}^k \chi^J(\mathbf{x}) \Delta \boldsymbol{\sigma}^J \quad (14)$$

108 where  $\Delta\boldsymbol{\varepsilon}^J$  and  $\Delta\boldsymbol{\sigma}^J$  are the incremental strain and stress in the  $J$ -th cluster. Hence, equation (13) can be  
 109 simplified according to these relations as,

$$\Delta\boldsymbol{\varepsilon}^I + \sum_{J=1}^k \left[ \frac{1}{c^I |\Omega|} \int_{\Omega} \int_{\Omega} \chi^I(\mathbf{x}) \chi^J(\mathbf{x}') \boldsymbol{\Phi}^0(\mathbf{x}, \mathbf{x}') d\mathbf{x}' d\mathbf{x} \right] : [\Delta\boldsymbol{\sigma}^J - \mathbf{C}^0 : \Delta\boldsymbol{\varepsilon}^J] - \Delta\boldsymbol{\varepsilon}^0 = 0. \quad (15)$$

110 where the term within brackets is a well-defined quantity in micromechanical analysis of materials: the  
 111 interaction tensor  $\mathbf{D}^{IJ}$ ,

$$\mathbf{D}^{IJ} = \frac{1}{c^I |\Omega|} \int_{\Omega} \int_{\Omega} \chi^I(\mathbf{x}) \chi^J(\mathbf{x}') \boldsymbol{\Phi}^0(\mathbf{x}, \mathbf{x}') d\mathbf{x}' d\mathbf{x}, \quad (16)$$

112 written as an integral of Green's function  $\boldsymbol{\Phi}^0(\mathbf{x}, \mathbf{x}')$  in a RUC domain  $\Omega$  with periodic boundary conditions,  
 113 and where  $c^I$  is the volume fraction of the  $I$ -th cluster and  $|\Omega|$  is the volume of domain  $\Omega$ .

114 Equation (13) can then be re-written considering equation (16) as

$$\Delta\boldsymbol{\varepsilon}^I + \sum_{J=1}^k \mathbf{D}^{IJ} : [\Delta\boldsymbol{\sigma}^J - \mathbf{C}^0 : \Delta\boldsymbol{\varepsilon}^J] - \Delta\boldsymbol{\varepsilon}^0 = 0. \quad (17)$$

115 This is an integral equation for each  $I$ -th cluster, which can be used together with the previously defined  
 116 macro-strain or macro-stress constraints in incremental form:

$$\sum_{I=1}^k c^I \Delta\boldsymbol{\varepsilon}^I = \Delta\bar{\boldsymbol{\varepsilon}} \quad \text{or} \quad \sum_{I=1}^k c^I \Delta\boldsymbol{\sigma}^I = \Delta\bar{\boldsymbol{\sigma}}, \quad (18)$$

117 **Remark 1.** *The system of equations composed by  $k$  equations (17) and the respective constraint equations*  
 118 *(18) is the main result of this section. This closed system of equations arises from the averaging of the*  
 119 *Lippmann-Schwinger equation for each cluster.*

120 Note that equations (17) and (18) do not depend on the strain concentration tensor or on any additional  
 121 parameters or constitutive laws. This contrasts with approaches such as TFA [22] and NTFA [23, 39]. Also  
 122 note that the separate averaging of the Lippmann-Schwinger equation introduced in this section implies that  
 123 stresses in adjacent clusters are not enforced to be continuous, but the global average of the local strains and  
 124 stresses are constrained to coincide with the macroscopic applied strain or stress. In a way, this is similar to  
 125 what happens in the finite element discretization of the conservation of linear momentum equation where  
 126 the continuity of stresses is also not enforced between adjacent elements, but global equilibrium is satisfied.

127 The system of equations (17-18) requires the previous determination of the material clusters (domain  
 128 decomposition), followed by the computation of the interaction tensors  $\mathbf{D}^{IJ}$  between each pair of clusters.  
 129 This *a priori* analysis is conveniently called the “offline” or training stage. The “online” or predictive stage  
 130 comprises the actual solution of the system of equations (17-18) for any loading conditions applied to the  
 131 RUC. Section 2.2 describes the offline stage, where a strategy to find the reduced RUC previously mentioned  
 132 is proposed. Section 2.3 presents the details of the online stage. Figure 2 shows a schematic of the developed  
 133 framework summarizing the methodology.

## 134 2.2. Offline stage

135 How can one perform the domain decomposition in the “offline stage”? Different methodologies can  
 136 be adopted. The goal is to group points that have similar mechanical behavior under any applied loading  
 137 condition. An optimal strategy to find the material clusters is proposed next by using a data compression  
 138 algorithm called k-means clustering.

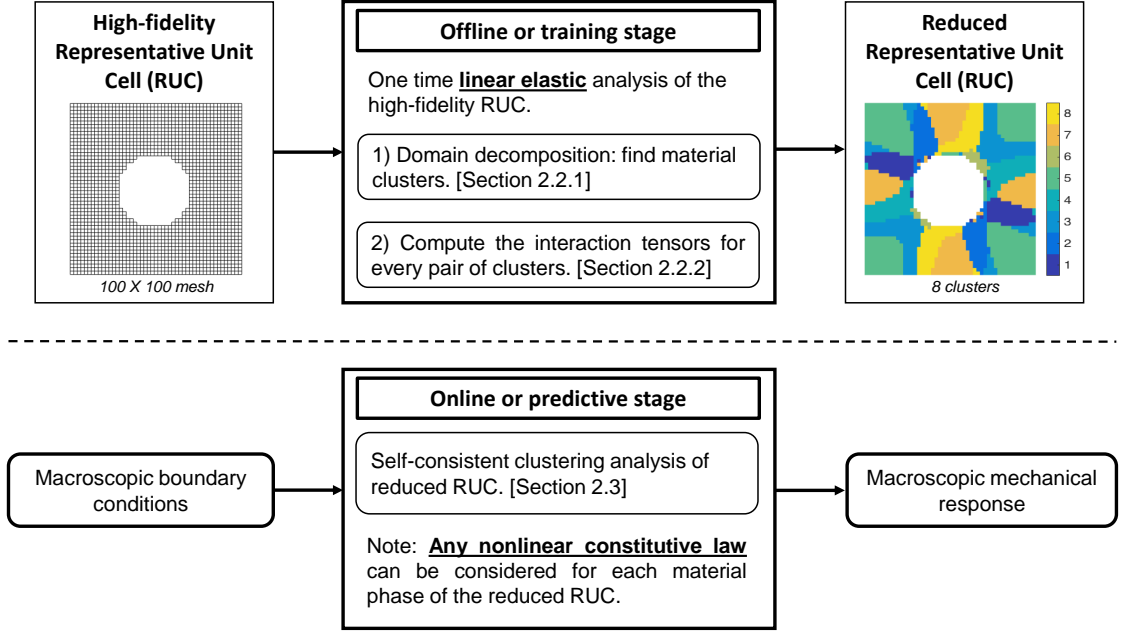


Figure 2: Flowchart summarizing the self-consistent clustering analysis developed in this work. Compared to other reduced order models the offline stage is trivial because it only involves a linear elastic analysis of the representative unit cell (RUC).

139 *2.2.1. Domain decomposition via k-means clustering*

140 A simple yet effective way of characterizing points in the material with similar mechanical behavior  
 141 is by evaluating the **elastic** response of the high-fidelity RUC and computing at every point the strain  
 142 concentration tensor  $\mathbf{A}(\mathbf{x})$ . This tensor relates the elastic microscopic strain  $\boldsymbol{\varepsilon}^{\text{micro}}(\mathbf{x})$  to the homogeneous  
 143 elastic macroscopic strain  $\boldsymbol{\varepsilon}^{\text{macro}}$ ,

$$\boldsymbol{\varepsilon}^{\text{micro}}(\mathbf{x}) = \mathbf{A}(\mathbf{x}) : \boldsymbol{\varepsilon}^{\text{macro}}, \quad (19)$$

144 where the macroscopic strain  $\boldsymbol{\varepsilon}^{\text{macro}}$  is directly related to the periodic boundary conditions of the RUC [12].

145 By definition, the similarity between two data points is characterized by the difference between their  
 146 strain concentration tensors. In other words, if two data points have equivalent strain concentration tensors,  
 147 they have exactly the same mechanical behavior under any loading condition within the elastic regime.  
 148 Moreover, these points should also have similar nonlinear plastic response, since the localization of plasticity  
 149 occurs at points with high strain concentrations.

150 For a 2-dimensional (2D) material, the strain concentration tensor  $\mathbf{A}(\mathbf{x})$  in each material point has 9 in-  
 151 dependent components which are determined by direct numerical simulation (DNS) of the high-fidelity RUC  
 152 under 3 orthogonal loading conditions. While for a 3-dimensional (3D) material,  $\mathbf{A}(\mathbf{x})$  has 36 independent  
 153 components, needing a set of DNS under 6 orthogonal loading conditions. The format of the raw data for  
 154 a 2D material is shown below,

DataIndex	$A_{11}$	$A_{22}$	$A_{33}$	$A_{12}$	$A_{21}$	$A_{23}$	$A_{32}$	$A_{13}$	$A_{31}$
1	-	-	-	-	-	-	-	-	-
2	-	-	-	-	-	-	-	-	-
$\vdots$			$\vdots$			$\vdots$			$\vdots$
$N$	-	-	-	-	-	-	-	-	-

155 where the dimension of the data is 9 in the 2D case, and  $N$  is the total number of discretization points in the

156 DNS. For example, if the high-fidelity RUC is discretized by a  $600 \times 600$  finite element mesh with reduced  
 157 integration elements, then  $N$  is equal to  $3.6 \times 10^5$ .

158 **Remark 2.** *Understanding the above selection for measuring mechanical similarity is crucial. Other metrics*  
 159 *for similarity could be used but that would have direct effects on the reduction of the number of degrees of*  
 160 *freedom by forming material clusters. For example, a simpler metric would be to group data points according*  
 161 *to their spatial proximity (disregarding their mechanical similarity), as was done later in this article for*  
 162 *comparison (Figure 6).*

163 The next step is to perform the domain decomposition by grouping similar data points using a clustering  
 164 algorithm called k-means clustering [43]. Note that the data points grouped by the k-means clustering  
 165 do not need to be adjacent to each other. These points belong to the same cluster because their strain  
 166 concentration tensor is approximately the same, but they can be in disconnected parts of the RUC – see  
 167 in Figure 3 irregular and disconnected clusters represented by the same color for two different material  
 168 microstructures.

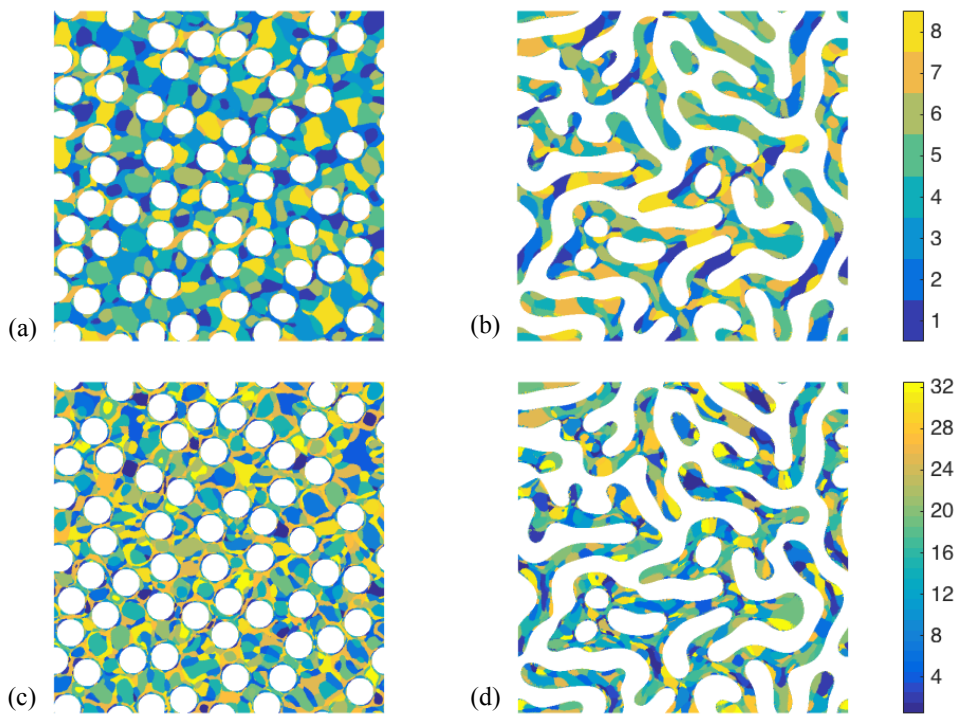


Figure 3: Two-dimensional k-means clustering results of (a,c) the cross-section of a fiber-reinforced composite with identical circular inclusions embedded in a matrix material and (b,d) a two-phase amorphous structure from a two-dimensional phase-field simulation based on the Cahn-Hilliard equation [44]. For both microstructures, phase 1 (matrix) was discretized into **8 clusters** in (a,b) and **32 clusters** in (c,d), while the discretization of phase 2 is not shown here for clarity. Note that **one** cluster is a group of **separate** subdomains indicated by the same color.

169 Figure 3a) and b) show the reduced RUC domain decomposition considering only 8 clusters for the  
 170 matrix phase, while figures c) and d) were obtained considering 32 clusters for the same phase. Regions  
 171 with the same color represent the same cluster. Recall that the methodology proposed in this work assumes  
 172 that the local variables in each cluster are uniform. Therefore, in this example the finite element mesh of the  
 173 high-fidelity RUC that had three hundred and sixty thousand elements was reduced to a few clusters (8 or  
 174 32) that can be used to solve the system of equations (17-18). This represents an extensive data compression  
 175 that is expected to lead to tremendous computational savings in the posterior online stage.

176 Clustering methods have been widely applied to different fields, from pattern recognition and image seg-  
 177 mentation to bioinformatics [45, 46]. Recently, a large spectrum of clustering algorithms has been developed,  
 178 such as hierarchical clustering, k-means clustering and distribution-based clustering [47]. In this manuscript,  
 179 a particular kind of centroid-based clustering named k-means clustering [43] is applied to compress the data.

180 In k-means clustering all the data points are partitioned into  $k$  clusters in the following manner:

- 181 1. Evaluate the quantity of interest (e.g, strain-concentration tensor) at each point in the domain;
- 182 2. Group all the points into  $k$  clusters such that the difference between the quantity of interest at each  
 183 point within the cluster is minimal when compared to the average value of that quantity inside that  
 184 cluster.

185 For the case of the RUC, the suggested quantity of interest is the strain concentration tensor. Hence, this  
 186 means that a cluster  $J$  contains the points whose strain concentration tensor  $\mathbf{A}(\mathbf{x})$  is closer to the average  
 187 strain concentration tensor of that cluster  $\bar{\mathbf{A}}_J$  when compared to the average strain concentration tensor  $\bar{\mathbf{A}}_I$   
 188 of any other cluster  $I$  (for  $I \neq J$ ). Once again it is noted that the clusters are not necessarily of the same  
 189 size and do not need to be continuous, see Figure 3.

190 Mathematically, given a set of strain concentration tensors the objective of k-means clustering is to  
 191 minimize the within-cluster least squares sum for the  $k$  sets  $\mathbf{S} = \{S^1, S^2, \dots, S^k\}$  to obtain the shape of the  
 192 clusters:

$$\mathbf{S} = \underset{\mathbf{S}'}{\operatorname{argmin}} \sum_{J=1}^k \sum_{n \in S^J} \|\mathbf{A}_n - \bar{\mathbf{A}}_J\|^2, \quad (20)$$

193 where  $\mathbf{A}_n$  is the strain concentration tensor of the  $n$ -th data point, and  $\bar{\mathbf{A}}_J$  is the mean of all the strain  
 194 concentration tensors at the points within the cluster  $S_J$ . The above norm is defined as usual, e.g. for a  
 195 general second-order matrix  $\mathbf{Z}$  of dimension  $m \times m$

$$\|\mathbf{Z}\| = \sqrt{\sum_{i=1}^m \sum_{j=1}^m z_{ij}^2} = \sqrt{\operatorname{trace}(\mathbf{Z}^T \mathbf{Z})}, \quad (21)$$

196 and is called the Frobenius norm of matrix  $\mathbf{Z}$ .

197 The algorithms for solving the k-means clustering problem are well developed, such as the standard  
 198 algorithm (Lloyd’s algorithm) [48] or fast k-means clustering algorithm proposed by Kanungo *et al.* [49].  
 199 In this article the standard algorithm was used, with more details provided in Appendix A. Note that the  
 200 choice of the number of clusters  $k$  defines the degree of data compression achieved.

201 Mathematically, the “Silhouette Index” [50] can be used to measure the quality of clustering; however,  
 202 this may not be sufficient when considering the predictions of the mechanical behavior. Typically, a larger  
 203 number of clusters (larger  $k$ ) used in the offline stage leads to more accurate predictions in the online stage  
 204 since more information was stored, but the number of degrees of freedom increases correspondingly. The  
 205 computational cost associated with this increase is discussed in later sections. As a result, the choice for the  
 206 number of clusters should keep a balance between the compression ratio of the data set and the accuracy of  
 207 the prediction.

208 **Remark 3.** *Clustering depends on specific choices of data type (in this case, strain concentration tensor),*  
 209 *distance definition (Frobenius norm) and clustering algorithm (k-means clustering). Other selections could*  
 210 *be made with direct influence on the mechanical behavior predicted. This exploratory effort is expected to be*  
 211 *conducted in future studies.*

### 212 2.2.2. Computing the interaction tensors

213 After the domain decomposition that determines the material clusters, one needs to compute the inter-  
 214 action tensors between clusters. The interaction tensor  $\mathbf{D}^{IJ}$  represents the influence of the stress in the  $J$ -th



215 cluster on the strain in the  $I$ -th cluster. As mentioned previously, the interaction tensor can be written as  
 216 an integral of Green's function in a RUC domain  $\Omega$  with periodic boundary conditions,

$$\mathbf{D}^{IJ} = \frac{1}{c^I |\Omega|} \int_{\Omega} \int_{\Omega} \chi^I(\mathbf{x}) \chi^J(\mathbf{x}') \Phi^0(\mathbf{x}, \mathbf{x}') d\mathbf{x}' d\mathbf{x}, \quad (22)$$

217 where  $c^I$  is the volume fraction of the  $I$ -th cluster and  $|\Omega|$  is the volume of domain  $\Omega$ .  $\Phi^0(\mathbf{x}, \mathbf{x}')$  is the  
 218 fourth-order periodic Green's function associated with an isotropic linear elastic reference material with  
 219 stiffness tensor  $\mathbf{C}^0$ . The definition and function of the reference material is discussed in Section 2.3. Also  
 220 note that the interaction tensor  $\mathbf{D}^{IJ}$  has to be a fourth-order tensor. In addition, by inspection of equation  
 221 (16), it can be seen that

$$c^I \mathbf{D}^{IJ} = c^J \mathbf{D}^{JI}. \quad (23)$$

222 When the reference material is linear elastic (including isotropic and anisotropic), the Green's function  
 223 is explicitly known in Fourier (frequency) space. For simplicity, we restrict the reference material to be  
 224 isotropic linear elastic in this article, so that its Green's function takes the following form in Fourier space,

$$\hat{\Phi}_{ijkl}^0(\boldsymbol{\xi}) = \frac{1}{4\mu^0 |\boldsymbol{\xi}|^2} (\delta_{ik} \xi_j \xi_l + \delta_{il} \xi_j \xi_k + \delta_{jl} \xi_i \xi_k + \delta_{jk} \xi_i \xi_l) - \frac{\lambda^0 + \mu^0}{\mu^0 (\lambda^0 + 2\mu^0)} \frac{\xi_i \xi_j \xi_k \xi_l}{|\boldsymbol{\xi}|^4}, \quad (24)$$

225 where  $\boldsymbol{\xi}$  is the coordinate in Fourier space corresponding to  $\mathbf{x}$  in real space,  $\lambda^0$  and  $\mu^0$  are Lamé constants of  
 226 the reference material. The formulation in equation (24) works for both 2D plane strain and 3D materials.  
 227 For convenience, the Green's function  $\hat{\Phi}_{ijkl}^0(\boldsymbol{\xi})$  can be rewritten in two parts:

$$\hat{\Phi}^0(\boldsymbol{\xi}) = \frac{1}{4\mu^0} \hat{\Phi}^1(\boldsymbol{\xi}) + \frac{\lambda^0 + \mu^0}{\mu^0 (\lambda^0 + 2\mu^0)} \hat{\Phi}^2(\boldsymbol{\xi}) \quad (25)$$

228 where each part can be written as

$$\hat{\Phi}_{ijkl}^1(\boldsymbol{\xi}) = \frac{1}{|\boldsymbol{\xi}|^2} (\delta_{ik} \xi_j \xi_l + \delta_{il} \xi_j \xi_k + \delta_{jl} \xi_i \xi_k + \delta_{jk} \xi_i \xi_l) \quad \text{and} \quad \hat{\Phi}_{ijkl}^2(\boldsymbol{\xi}) = -\frac{\xi_i \xi_j \xi_k \xi_l}{|\boldsymbol{\xi}|^4}, \quad (26)$$

229 Since  $\hat{\Phi}^1(\boldsymbol{\xi})$  and  $\hat{\Phi}^2(\boldsymbol{\xi})$  do not depend on the material properties, only the coefficients before them need  
 230 to be updated if the elastic constants  $\lambda^0$  and  $\mu^0$  of the reference material change. This feature of  $\hat{\Phi}^0(\boldsymbol{\xi})$   
 231 is essential to the self-consistent scheme as introduced in Section 2.3. Moreover, the convolution term in  
 232 equation (16) can be translated into a direct multiplication based on a Fourier transformation,

$$\int_{\Omega} \chi^I(\mathbf{x}') \Phi^0(\mathbf{x}, \mathbf{x}') d\mathbf{x}' = \mathcal{F}^{-1} \left( \hat{\chi}^I(\boldsymbol{\xi}) \hat{\Phi}^0(\boldsymbol{\xi}) \right) \quad (27)$$

233 where  $\hat{\chi}^I(\boldsymbol{\xi})$  is the characteristic function in the  $I$ -th cluster in the Fourier space. Only a one-time calculation  
 234 is needed for computing all the interaction tensors, which can then be used for considering complex material  
 235 behavior.

### 236 2.3. Online stage: Self-consistent clustering analysis

237 If an actual prediction of the local strains in the RUC for any constitutive behavior of the phases is to  
 238 be obtained, then two points still need to be discussed: 1) the choice of the reference material stiffness  $\mathbf{C}^0$ ;  
 239 and 2) the algorithmic details to find the iterative solution for equations (17) and (18).

240 Concerning the first point, it is highlighted that the local strain  $\boldsymbol{\varepsilon}(\mathbf{x})$  solved from the **continuous**  
 241 Lippmann-Schwinger equation, i.e. equation (8) or (12), does not depend on the choice of  $\mathbf{C}^0$ . On the  
 242 other hand, the choice of  $\mathbf{C}^0$  affects the convergence rate of the iterative solution scheme for the discrete  
 243 Lippmann-Schwinger equation as pointed out in [19, 51, 52, 53]. Despite the influence on the convergence  
 244 rate, the converged solution reached by the discretized scheme should be the same and independent of the  
 245 choice of  $\mathbf{C}^0$ , which could be regarded as a preconditioner of the iterative scheme. This can be explained by

246 the fact that the physical problem is completely determined by the equilibrium condition and macroscopic  
 247 constraints. The far-field strain  $\boldsymbol{\varepsilon}^0$  in those equations just assumes a different value according to the choice  
 248 of  $\mathbf{C}^0$  such that the same solution for the local strain in the RUC is obtained. Therefore, *in theory* one can  
 249 choose any reference stiffness  $\mathbf{C}^0$  for the homogeneous linear elastic material. In practice, this is not the  
 250 case – see Remark 4.

251 **Remark 4.** *The solution of the **discrete** Lippmann-Schwinger equations when finding the local strain in*  
 252 *each cluster by solving equations (17) and (18) is actually affected by the choice of the reference stiffness*  
 253  *$\mathbf{C}^0$ .*

254 Section 2.3.1 presents the algorithmic details to solve the discrete equations (17) and (18) considering  
 255 a constant  $\mathbf{C}^0$  first. Then, in Section 2.3.2, a discussion of the importance of a self-consistent scheme for  
 256 updating  $\mathbf{C}^0$  upon deformation is presented.

### 257 2.3.1. Algorithm for constant $\mathbf{C}^0$

258 In general cases such as plasticity and damage, the incremental stress in the  $I$ -th cluster  $\Delta\boldsymbol{\sigma}^I$  is a  
 259 nonlinear function of its incremental strain  $\Delta\boldsymbol{\varepsilon}^I$ , which means that the system of integral equations needs to  
 260 be solved iteratively at every load increment. An implicit scheme is adopted herein, and both macro-strain  
 261 and macro-stress constraints are considered.

262 As mentioned before, the unknown variables of the system are the incremental strain in each cluster  $\Delta\boldsymbol{\varepsilon}^I$   
 263 and the far field strain  $\Delta\boldsymbol{\varepsilon}^0$ , so  $\{\Delta\boldsymbol{\varepsilon}\} = \{\Delta\boldsymbol{\varepsilon}^1; \dots; \Delta\boldsymbol{\varepsilon}^k; \Delta\boldsymbol{\varepsilon}^0\}$ . To begin, the residual of the integral equation  
 264 in the  $I$ -th cluster at iteration step  $n$  is defined as

$$\mathbf{r}^I(\{\Delta\boldsymbol{\varepsilon}\}_n) = \Delta\boldsymbol{\varepsilon}_n^I + \sum_{J=1}^k \mathbf{D}^{IJ} : [\Delta\boldsymbol{\sigma}_n^J - \mathbf{C}^0 : \Delta\boldsymbol{\varepsilon}_n^J] - \Delta\boldsymbol{\varepsilon}_n^0 \quad \text{with } I = 1, 2, \dots, k, \quad (28)$$

265 and the residuals of the macro-strain or macro-stress constraints are

$$\mathbf{r}^{k+1}(\{\Delta\boldsymbol{\varepsilon}\}_n) = \sum_{I=1}^k c^I \Delta\boldsymbol{\varepsilon}_n^I - \Delta\bar{\boldsymbol{\varepsilon}} \quad \text{or} \quad \mathbf{r}^{k+1}(\{\Delta\boldsymbol{\varepsilon}\}_n) = \sum_{I=1}^k c^I \Delta\boldsymbol{\sigma}_n^I - \Delta\bar{\boldsymbol{\sigma}}. \quad (29)$$

266 In the implicit scheme, the residual  $\{\mathbf{r}\} = \{\mathbf{r}^1; \dots; \mathbf{r}^k; \mathbf{r}^{k+1}\}$  is linearized with respect to  $\{\Delta\boldsymbol{\varepsilon}\}$ . After  
 267 dropping terms of higher order than linear, it gives

$$\{\mathbf{r}\} + \{\mathbf{M}\}\{\delta\boldsymbol{\varepsilon}\} = \mathbf{0} \quad \text{with } \{\mathbf{M}\} = \frac{\partial\{\mathbf{r}\}}{\partial\{\Delta\boldsymbol{\varepsilon}\}}, \quad (30)$$

268 where  $\{\mathbf{M}\}$  is called the system Jacobian matrix. For  $I, J = 1, 2, \dots, k$ , we have

$$\mathbf{M}^{IJ} = \delta_{IJ}\mathbf{I} + \mathbf{D}^{IJ} : \left(\mathbf{C}_{alg}^J - \mathbf{C}^0\right) \quad \text{and} \quad \mathbf{M}^{I(k+1)} = -\mathbf{I}, \quad (31)$$

269 where  $\delta_{IJ}$  is the Kronecker delta in terms of indices  $I$  and  $J$ , and  $\mathbf{I}$  is the fourth-order identity tensor.  
 270  $\mathbf{C}_{alg}^J$  is the so-called algorithmic modulus (or tangent modulus) of the material in the  $J$ -th cluster and is an  
 271 output of the local constitutive law for the current strain increment in that cluster  $\Delta\boldsymbol{\varepsilon}_n^J$ ,

$$\mathbf{C}_{alg}^J = \frac{\partial\Delta\boldsymbol{\sigma}^J}{\partial\Delta\boldsymbol{\varepsilon}^J}. \quad (32)$$

272 Under the macro-strain constraint, the remaining components in the system Jacobian matrix are

$$\mathbf{M}^{(k+1)I} = c^I\mathbf{I} \quad \text{and} \quad \mathbf{M}^{(k+1)(k+1)} = \mathbf{0}. \quad (33)$$

273 For macro-stress constraint, we have

$$\mathbf{M}^{(k+1)I} = c^I\mathbf{C}_{alg}^I \quad \text{and} \quad \mathbf{M}^{(k+1)(k+1)} = \mathbf{0}. \quad (34)$$

274 Finally, the correction of the incremental strain can be expressed as

$$\{\delta\boldsymbol{\varepsilon}\} = -\{\mathbf{M}\}^{-1}\{\mathbf{r}\}. \quad (35)$$

275 Based on the updated incremental strain, we can then use the constitutive relationship in each cluster to  
 276 compute the new incremental stress  $\{\Delta\boldsymbol{\sigma}\} = \{\Delta\boldsymbol{\sigma}^1; \dots; \Delta\boldsymbol{\sigma}^k\}$ . The algorithm for the implicit scheme is given  
 277 in the box below, where it is again highlighted that the constant  $\mathbf{C}^0 = \mathbf{C}^{\text{input}}$  is chosen by the analyst as  
 278 an input  $\mathbf{C}^{\text{input}}$ . The most logic choice is to consider as reference the effective stiffness of the RUC that  
 279 can be determined in the offline stage  $\mathbf{C}^{\text{input}} = \mathbf{C}^{\text{macro}}$ . However, as previously mentioned, other reference  
 280 stiffnesses could be considered, e.g. the stiffness of the matrix phase  $\mathbf{C}^{\text{input}} = \mathbf{C}^{\text{matrix}}$ .

**Box 2.1 Algorithm for the implicit scheme with constant  $\mathbf{C}^0$**

1. Initial conditions and initialization: set  $\{\Delta\boldsymbol{\varepsilon}\}_0 = \mathbf{0}; n = 0; \{\Delta\boldsymbol{\varepsilon}\}_{\text{new}} = \{\Delta\boldsymbol{\varepsilon}\}_0; \mathbf{C}^0 = \mathbf{C}^{\text{input}}$
2. Newton iterations for load increment  $n + 1$ :
  - a. compute the incremental stress  $\{\Delta\boldsymbol{\sigma}\}_{\text{new}}$  based on material constitutive laws
  - b. use 28 and 29 to compute the residual  $\{\mathbf{r}\} = \mathbf{f}(\{\Delta\boldsymbol{\varepsilon}\}_{\text{new}}, \{\Delta\boldsymbol{\sigma}\}_{\text{new}})$
  - c. compute the system Jacobian  $\{\mathbf{M}\}$
  - d. solve the linear equation  $\{\delta\boldsymbol{\varepsilon}\} = -\{\mathbf{M}\}^{-1}\{\mathbf{r}\}$
  - e.  $\{\Delta\boldsymbol{\varepsilon}\}_{\text{new}} \leftarrow \{\Delta\boldsymbol{\varepsilon}\}_{\text{new}} + \{\delta\boldsymbol{\varepsilon}\}$
  - f. check error criterion; if not met, go to 2a.
3. Update the incremental strain and stress:  $\{\Delta\boldsymbol{\varepsilon}\}_{n+1} = \{\Delta\boldsymbol{\varepsilon}\}_{\text{new}}, \{\Delta\boldsymbol{\sigma}\}_{n+1} = \{\Delta\boldsymbol{\sigma}\}_{\text{new}}; n \leftarrow n + 1$
4. If simulation not complete, go to 2.

282 *2.3.2. Algorithm with self-consistent  $\mathbf{C}^0$*

283 Remark 4 highlights that due to the discrete character of the approach the actual choice of the stiffness  
 284 of the reference material  $\mathbf{C}^0$  can affect the solution, contrary to what happens for the continuous form. This  
 285 raises a question: Is there an optimal choice for  $\mathbf{C}^0$ ?

286 Here a self-consistent scheme is proposed to set the homogeneous tangent modulus of the reference  
 287 material  $\mathbf{C}^0$  approximately the same as the macroscopic tangent modulus (i.e. the effective tangent modulus  
 288 of the RUC) even **after** plastic deformation occurs,

$$\mathbf{C}^0 \rightarrow \mathbf{C}^{\text{macro}}. \quad (36)$$

289 Let's start by considering the elastic case first, where the effective tangent modulus of the RUC does not  
 290 change and coincides with the effective elastic stiffness of the RUC. By averaging the incremental integral  
 291 equation 12 in the RUC domain  $\Omega$ , we have

$$\Delta\boldsymbol{\varepsilon}^{\text{macro}} + \frac{1}{|\Omega|} \int_{\Omega} \left( \int_{\Omega} \boldsymbol{\Phi}^0(\mathbf{x}, \mathbf{x}') d\mathbf{x} \right) : [\Delta\boldsymbol{\sigma}(\mathbf{x}') - \mathbf{C}^{\text{macro}} : \Delta\boldsymbol{\varepsilon}(\mathbf{x}')] d\mathbf{x}' - \Delta\boldsymbol{\varepsilon}^0 = 0. \quad (37)$$

292 According to the definition of periodic Green's function  $\boldsymbol{\Phi}^0(\mathbf{x}, \mathbf{x}')$ , the following integral results in a  
 293 constant tensor which does not depend on  $\mathbf{x}'$ ,

$$\int_{\Omega} \boldsymbol{\Phi}^0(\mathbf{x}, \mathbf{x}') d\mathbf{x} = \mathbf{S} : (\mathbf{C}^0)^{-1}, \quad (38)$$

294 where  $\mathbf{S}$  is the Eshelby's tensor. By substituting equation (38) into (37), the following statement can be  
 295 proved,

$$\Delta\boldsymbol{\varepsilon}^0 = \Delta\boldsymbol{\varepsilon}^{\text{macro}}, \quad \text{if } \mathbf{C}^0 = \mathbf{C}^{\text{macro}}. \quad (39)$$

296 This result can be extrapolated to the case of irreversible processes such as plasticity. For a given  
 297 increment  $n$ , when  $\mathbf{C}_n^0$  tends to the tangent modulus of the RUC  $\mathbf{C}_n^{\text{macro}}$ , then the far-field strain  $\Delta\boldsymbol{\varepsilon}_n^0$  tends  
 298 to the macroscopic strain  $\Delta\boldsymbol{\varepsilon}_n^{\text{macro}}$ . Hence, the name **self-consistent** reference tangent modulus.

299 For convenience, however, the tangent modulus  $\mathbf{C}_n^{\text{macro}}$  is considered as isotropic even during plasticity  
 300 in order to still use the same form of Green's functions, see equation (24). This is not true in general, since  
 301 the plastic flow may introduce anisotropic behavior, especially under large deformations.

302 Considering the reference tangent modulus as isotropic at every macroscopic load increment, the self-  
 303 consistent scheme then needs to find the two independent Lamé parameters  $\lambda_n^0$  and  $\mu_n^0$  for every load  
 304 increment  $n$  that define  $\mathbf{C}_n^0$ ,

$$\mathbf{C}_n^0 = \mathbf{f}(\lambda_n^0, \mu_n^0), \quad (40)$$

305 such that the reference tangent modulus is closest to the macroscopic tangent modulus. The objective of  
 306 the self-consistent scheme is then to find  $\lambda_n^0$  and  $\mu_n^0$  from the following minimization,

$$\{\lambda_n^0, \mu_n^0\} = \underset{\{\lambda', \mu'\}}{\operatorname{argmin}} \|\Delta\boldsymbol{\sigma}_n^{\text{macro}} - \mathbf{f}(\lambda', \mu') : \Delta\boldsymbol{\varepsilon}_n^{\text{macro}}\|^2, \quad (41)$$

307 where  $\|\mathbf{Z}\|^2 = \mathbf{Z} : \mathbf{Z}$  for an arbitrary second-order tensor  $\mathbf{Z}$ . The macroscopic strain  $\boldsymbol{\varepsilon}_n^{\text{macro}}$  and stress  
 308  $\boldsymbol{\sigma}_n^{\text{macro}}$  at increment  $n$  are given by

$$\Delta\boldsymbol{\varepsilon}_n^{\text{macro}} = \sum_{I=1}^k c^I \Delta\boldsymbol{\varepsilon}_n^I \quad \text{and} \quad \Delta\boldsymbol{\sigma}_n^{\text{macro}} = \sum_{I=1}^k c^I \Delta\boldsymbol{\sigma}_n^I. \quad (42)$$

309 Then the optimum point  $(\lambda_{\text{opt}}^0, \mu_{\text{opt}}^0)$  is found by computing the minimum of  $g(\lambda_n^0, \mu_n^0)$ ,

$$g(\lambda_n^0, \mu_n^0) = \|\Delta\boldsymbol{\sigma}_n^{\text{macro}} - \mathbf{f}(\lambda_n^0, \mu_n^0) : \Delta\boldsymbol{\varepsilon}_n^{\text{macro}}\|^2 \quad (43)$$

310 via the respective partial derivatives,

$$\left. \frac{\partial g}{\partial \lambda_n^0} \right|_{\lambda_{\text{opt}}^0, \mu_{\text{opt}}^0} = 0 \quad \text{and} \quad \left. \frac{\partial g}{\partial \mu_n^0} \right|_{\lambda_{\text{opt}}^0, \mu_{\text{opt}}^0} = 0, \quad (44)$$

311 which basically forms a system of two linear equations in terms of the Lamé constants. The system always  
 312 has a unique solution except under a pure-shear loading condition, where  $\lambda_{\text{opt}}^0$  is underdetermined. In this  
 313 case, the value of  $\lambda_n^0$  is not updated. Additionally,  $g(\lambda_{\text{opt}}^0, \mu_{\text{opt}}^0)$  vanishes when the effective macroscopic  
 314 homogeneous material is also isotropic linear elastic.

315 This self-consistent scheme is also iterative, since the macroscopic incremental stress  $\Delta\boldsymbol{\sigma}_{\text{new}}^{\text{macro}}$  and strain  
 316  $\Delta\boldsymbol{\varepsilon}_{\text{new}}^{\text{macro}}$  at the beginning of the increment are computed based on previous values of  $\lambda_n^0$  and  $\mu_n^0$ . Note that  
 317 in the algorithm that uses a constant  $\mathbf{C}^0$ , see **Box 2.1**, since the tangent modulus  $\mathbf{C}^0$  is not updated that  
 318 implies that the interaction tensors  $\mathbf{D}^{IJ}$  also do not need to be updated. This is no longer the case for the  
 319 self-consistent algorithm, as presented in **Box 2.2**, since the interaction tensors given by equation (16) also  
 320 depend on the updated reference Lamé parameters following equation (24). It is also noted that for the  
 321 simulations considered in this work, the convergence of  $\lambda^0$  and  $\mu^0$  can be reached within a small number of  
 322 iterations (e.g. less than 5 for a tolerance 0.1%).

**Box 2.2 Algorithm for the updated self-consistent implicit scheme**

1. Initial conditions and initialization: set  $(\lambda^0, \mu^0)$ ;  $\{\Delta\boldsymbol{\varepsilon}\}_0 = \mathbf{0}$ ;  $n = 0$ ;  $\{\Delta\boldsymbol{\varepsilon}\}_{\text{new}} = \{\Delta\boldsymbol{\varepsilon}\}_0$
2. For load increment  $n + 1$ , update the interaction tensor  $\mathbf{D}^{IJ}$  and the stiffness tensor  $\mathbf{C}^0$
3. Newton iterations:
  - a. compute the incremental stress  $\{\Delta\boldsymbol{\sigma}\}_{\text{new}}$
  - b. use 28 and 29 to compute the residual  $\{\mathbf{r}\} = \mathbf{f}(\{\Delta\boldsymbol{\varepsilon}\}_{\text{new}}, \{\Delta\boldsymbol{\sigma}\}_{\text{new}})$
  - c. compute the system Jacobian  $\{\mathbf{M}\}$
  - d. solve the linear equation  $\{\delta\boldsymbol{\varepsilon}\} = -\{\mathbf{M}\}^{-1}\{\mathbf{r}\}$
  - e.  $\{\Delta\boldsymbol{\varepsilon}\}_{\text{new}} \leftarrow \{\Delta\boldsymbol{\varepsilon}\}_{\text{new}} + \{\delta\boldsymbol{\varepsilon}\}$
  - f. check error criterion; if not met, go to 3a.
4. Solve 44, and  $(\lambda^0, \mu^0) \leftarrow (\lambda_{\text{opt}}^0, \mu_{\text{opt}}^0)$
5. Check error criterion; if not met, go to 2
6. Update the incremental strain and stress:  $\{\Delta\boldsymbol{\varepsilon}\}_{n+1} = \{\Delta\boldsymbol{\varepsilon}\}_{\text{new}}$ ,  $\{\Delta\boldsymbol{\sigma}\}_{n+1} = \{\Delta\boldsymbol{\sigma}\}_{\text{new}}$ ;  $n \leftarrow n + 1$
7. If simulation not complete, go to 2.

With this last update we obtained a “self-consistent Lippmann-Schwinger multiple-cluster homogenization scheme” made computationally efficient by the data compression treatment proposed in Section 2.2.1 where clusters (subdomains) of material with similar mechanical properties were determined. The self-consistency of the proposed scheme is optional, i.e. it is possible to use a constant reference stiffness tensor  $\mathbf{C}^0$ . However, the convergence of the scheme is improved as shown next. We note that the scheme is standalone: there are no additional parameters nor evolution laws, unlike the schemes reviewed in Section 1.

#### 2.4. Microstructure and material modeling

The proposed reduced order homogenization method was applied to 2D plane strain and 3D heterogeneous materials under different load cases. As detailed in the previous sections, the whole modeling framework can be divided into two stages: 1) offline stage; and 2) online stage.

In the 2D plane strain examples, two types of materials with different microstructures as shown in Figure 3 are analyzed. The first one is a composite material with identical circular fibers (phase 2) embedded in the matrix (phase 1), where the fiber volume fraction was considered as  $V_{f_2} = 30\%$ . The second 2D plane strain example is a two-phase material with microstructure obtained from a phase-field simulation based on the Cahn-Hilliard equation, where the volume fraction of either phase is equal to 50%. For convenience, the two types of materials are abbreviated as fiber-reinforced composite and amorphous material, respectively.

Two examples in 3D are also presented: one was chosen as a two-phase composite material with identical spherical inclusions embedded in the matrix (volume fraction of 20%), and the other as an amorphous material with a microstructure obtained from a 3D phase-field simulation (volume fraction of 50%). All the microstructures considered in the examples are periodic.

The same material properties are used in the 2D and 3D problems. For the linear elastic direct numerical simulations in the offline stage, the Young’s moduli and Poisson’s ratios of phase 1 and 2 are:

$$E_1 = 100 \text{ MPa}, \nu_1 = 0.3; \quad E_2 = 500 \text{ MPa}, \nu_2 = 0.19. \quad (45)$$

Figure 3 showed the data compression achieved for the two RUCs used in the 2D examples considering 8 or 32 clusters for phase 1 of the materials. Each reduced RUC obtained for a chosen number of clusters is then analyzed in the online stage. Note that the same reduced RUC can be used for predicting plastic behavior of the material with any local plasticity laws for each phase (no additional calibration needed). Therefore, the following examples considered two different plasticity laws in order to assess the predictive capabilities of the proposed approach.

Two plasticity laws were considered in the online stage for phase 1 (the matrix material). Both laws considered a von Mises yield surface,

$$f = \bar{\sigma} - \sigma_Y(\bar{\boldsymbol{\varepsilon}}) \leq 0, \quad (46)$$

355 where  $\bar{\sigma}$  is the von Mises equivalent stress, and the yield stress  $\sigma_Y$  is given by the chosen hardening law that  
 356 depends on the equivalent plastic strain  $\bar{\varepsilon}$ .

357 The first hardening law considered was piecewise linear and isotropic as follows,

$$\sigma_Y(\bar{\varepsilon}) = \begin{cases} 0.5 + 5\bar{\varepsilon} & \bar{\varepsilon} \in [0, 0.04) \\ 0.7 + 2\bar{\varepsilon} & \bar{\varepsilon} \in [0.04, \infty) \end{cases} \text{ MPa.} \quad (47)$$

358 The other hardening law considered was the following power-law,

$$\sigma_Y(\bar{\varepsilon}) = 0.1 + 0.3\bar{\varepsilon}^{0.4} \text{ MPa.} \quad (48)$$

359 The plasticity simulations were conducted under different loading conditions. For example, under uniaxial  
 360 tension the macroscopic strain  $\varepsilon_{11}$  is prescribed, and the macroscopic stresses vanish in all other directions:  
 361  $\sigma_{ij} = 0$  for  $i, j \neq 1$ . For pure shear loading condition,  $\gamma_{12}$  is imposed and the remaining stress-free conditions  
 362 are applied similarly.

363 The predictions given by the reduced order modeling, including macroscopic behavior and microscopic  
 364 stress/strain fields, are validated against high-fidelity direct numerical simulations (DNS) using the finite  
 365 element method with a fine mesh and imposing periodic boundary conditions. The computational efficiency  
 366 of the proposed method is discussed as well.

### 367 3. Results and discussion

#### 368 3.1. Two-dimensional linear elastic materials

369 Before evaluating the plastic predictions of the reduced RUC, the elastic description is considered first.  
 370 The importance of applying the self-consistent (SC) scheme for updating  $\mathbf{C}^0$  is discussed herein as well.

371 Figure 4 presents the RUC's transverse Young's moduli and Poisson's ratios predicted by the proposed  
 372 method with and without the self-consistent (SC) scheme as a function of the number of clusters chosen in  
 373 the offline stage. For the approach without the self-consistent scheme, i.e. considering a constant reference  
 374 stiffness  $\mathbf{C}^0$ , phase 1 (matrix) was considered as the reference material:  $\mathbf{C}^0 = \mathbf{C}^{\text{matrix}}$ . The number of  
 375 clusters in phase 1 is denoted as  $k_1$ , while  $k_2$  denotes the number of clusters in phase 2. In these examples  $k_2$   
 376 was defined according to the volume fractions of the phases: for the fiber-reinforced composite the number  
 377 of clusters in the fibers was chosen as approximately half the number of clusters in the matrix  $k_2 = \lceil k_1/2 \rceil$   
 378 (recall that  $V_{f_2} = 30\%$ ); and for the amorphous material both phases were discretized with the same number  
 379 of clusters  $k_2 = k_1$  (recall that  $V_{f_1} = 50\%$ ). All the predictions are normalized with respect to the results  
 380 of direct numerical simulations (DNS) obtained from a converged finite element analysis considering a fine  
 381 mesh of elements:

- 382 1. Fiber-reinforced composite:  $E_{\text{DNS}} \approx 156.4 \text{ MPa}$ ,  $\nu_{\text{DNS}} \approx 0.39$ ;
- 383 2. Amorphous material:  $E_{\text{DNS}} \approx 220.8 \text{ MPa}$ ,  $\nu_{\text{DNS}} \approx 0.35$ .

384 Observing the figure there is an immediate characteristic of the presented solutions: the accuracy of  
 385 the prediction improves by increasing the number of clusters in the system, as expected. Moreover, the  
 386 predictions for the effective  $E$  and  $\nu$  of the RUC for the fiber-reinforced composite are similar with or  
 387 without the self-consistent (SC) scheme: both approaches converge within an error tolerance of 1% after  
 388 assigning 8 clusters in phase 1 (matrix). However, convergence is significantly faster with the self-consistent  
 389 scheme<sup>3</sup> for the amorphous material (both for  $E$  and  $\nu$ ). These results confirm Remark 4: since the  
 390 Lippmann-Schwinger equation is being numerically discretized instead of being solved exactly, the choice of  
 391 the reference material affects the convergence of the solution. This was also pointed out by Chaboche et al.  
 392 [39] in their complete analysis of the capabilities of mean-field approaches.

---

<sup>3</sup>For the linear-elastic examples, the self-consistent scheme finds  $\mathbf{C}^0$  to be the same as the effective stiffness of the RUC  $\mathbf{C}^{\text{macro}}$ . So, considering  $\mathbf{C}^{\text{input}} = \mathbf{C}^{\text{macro}}$  in the non self-consistent scheme of **Box 2.1** would lead to the same convergence as the self-consistent scheme (for linear elasticity only).

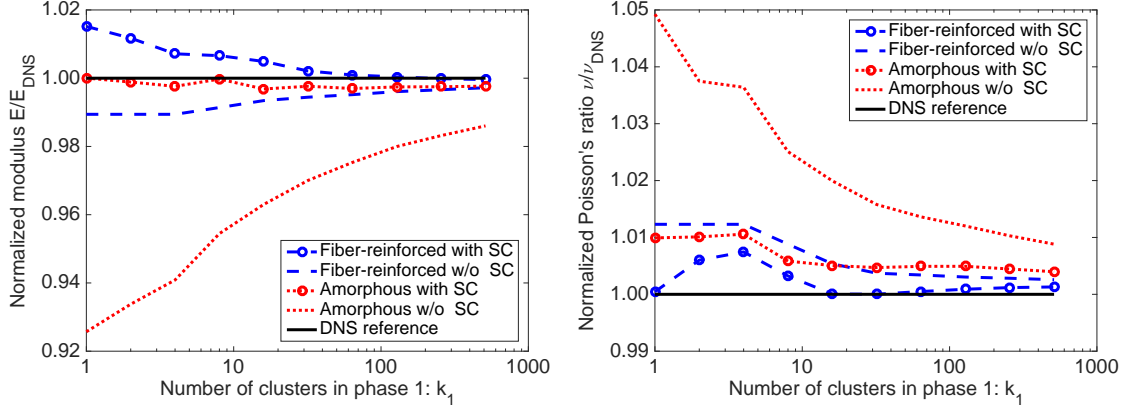


Figure 4: Normalized transverse Young modulus (left) and Poisson's ratio (right) as a function of the number of cluster in phase 1 (matrix). The DNS results for the fiber-reinforced composite and amorphous material were obtained from finite element analyses.

393 The predictive capabilities of the proposed method can be further assessed by considering the variation  
 394 of the elastic properties at the online stage without redoing the offline stage. The interested reader is  
 395 referred to Appendix B and Figure B.14, where new effective elastic properties of the RUC were reasonably  
 396 well predicted even when using new combinations of elastic properties for the two phases of the material  
 397 that differ from the ones used in the offline stage, equation (45). This shows the potential of applying  
 398 the proposed method to microstructure-based property design of heterogeneous material system, such as  
 399 nanostructured polymers [54].

### 400 3.2. Two-dimensional nonlinear elasto-plastic materials

401 Particularly relevant is the assessment of the predictive capabilities of the proposed model when capturing  
 402 the nonlinear plastic behavior of the RUC under various loading conditions, as well as the computational cost  
 403 (CPU time and memory) when compared to the DNS. First the influence of the self-consistent scheme on  
 404 the plastic predictions is investigated considering the two hardening laws introduced previously: the piece-  
 405 wise linear hardening, equation (47); and the power-law hardening, equation (48). Figure 5 presents the  
 406 stress-strain results for the fiber-reinforced composite subjected to uniaxial tension for these two hardening  
 407 laws of the matrix.

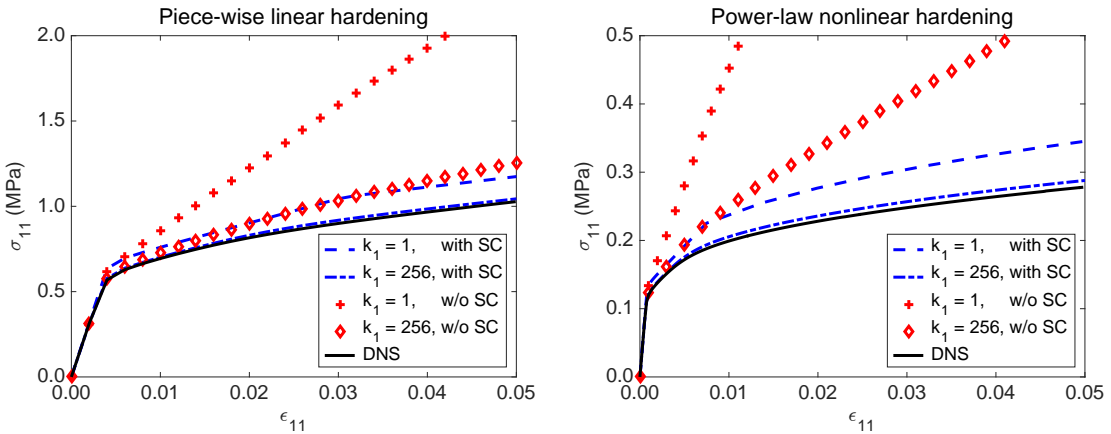


Figure 5: The effect of the self-consistent scheme on the plastic behavior of the fiber-reinforced material under piece-wise linear hardening (left) and power-law nonlinear hardening (right) loading conditions.

408 As can be observed in the figure, although the error of the method when compared to DNS is reduced in

409 each case by increasing the number of clusters, the self-consistent scheme converges significantly faster for  
 410 a desired level of accuracy. This is especially visible for the power-law nonlinear hardening. When plastic  
 411 yielding happens in the heterogeneous material, the macroscopic tangent stiffness tensor starts decreasing  
 412 when compared to the elastic case due to localized plasticity in the matrix, so that  $\mathbf{C}^{\text{matrix}}$  is no longer  
 413 a good choice for the tangent stiffness  $\mathbf{C}^0$  of the reference material. By consistently updating  $\mathbf{C}^0$  with  
 414 an approximate value of the effective stiffness of the RUC, see Box 2.2, the evolution of the local internal  
 415 variables in each cluster is captured more accurately.

416 Another point to be considered is the effect of the  $\mathbf{A}$ -based clustering used during the offline stage,  
 417 introduced in Section 2.2.1. As discussed in that section, the k-means clustering was done based on the  
 418 strain concentration tensor  $\mathbf{A}(\mathbf{x})$  at each data point, with the purpose of grouping the data points with  
 419 similar mechanical behavior into one cluster. A more naive compression scheme would be to do the clustering  
 420 purely based on the spatial coordinates  $\mathbf{x}$  of the data points, i.e. grouping points by their spatial proximity  
 421 instead of considering the similarity of mechanical behavior. This position-based clustering leads to a cluster  
 422 map resembling a Voronoi diagram, as illustrated in Figure 6 (left) for 32 clusters in phase 1 for the fiber-  
 423 reinforced composite. The reader is encouraged to compare this figure with Figure 3c) to see the difference  
 424 in the clustering scheme for the **same** number of clusters but using the  $\mathbf{A}$ -based clustering.

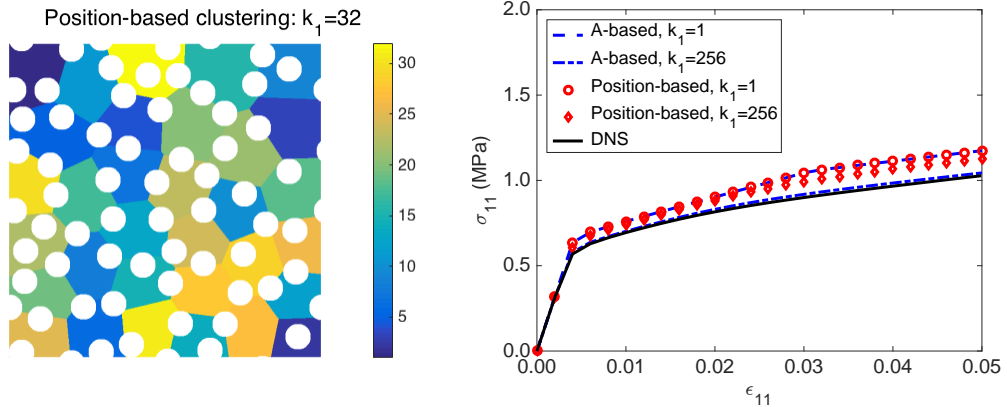


Figure 6: The effect of the raw data type on the clustering results (left), as well as the corresponding predictions on macroscopic response (right), for the fiber-reinforced composite under uniaxial tension. The position-based clustering results with 32 clusters are shown on the left.

425 On the right of Figure 6 the results of position-based clustering are compared to the  $\mathbf{A}$ -based clustering.  
 426 In this figure it is seen that the convergence using the position-based clusters is poor and the accuracy of  
 427 the prediction does not change significantly even considering 256 clusters for phase 1. On the contrary, with  
 428 the same number of clusters the predictions from  $\mathbf{A}$ -based clustering reproduce the DNS almost exactly.

429 Figure 7 includes the stress-strain curves for the fiber-reinforced composite and the amorphous material  
 430 considering two different load cases, uniaxial tension and pure shear, using the self-consistent scheme. The  
 431 number of clusters in phase 1 ranges from 1 to 256, and the results from DNS are also provided for compari-  
 432 son. By looking at the plots, we can conclude that the proposed method is capable of capturing the nonlinear  
 433 plastic behavior with significantly fewer degrees of freedom but with a small loss in accuracy. Furthermore,  
 434 the refinement of the discretization by including more clusters clearly improves the predictions: a desirable  
 435 characteristic allowing the analyst to choose between accuracy and efficiency.

436 Figure 8 provides a comparison of the local fields obtained from DNS of the high-fidelity RUC and from  
 437 the proposed self-consistent clustering analysis of a reduced RUC with 256 clusters for phase 1. The figures  
 438 show that the new method is able to reproduce the equivalent plastic strain fields, although the localized  
 439 regions are reproduced in a more diffuse manner leading to regions with lower strain concentrations. This  
 440 is expected since by definition the goal of the proposed approach is to predict as accurately as possible the  
 441 global (homogenized) mechanical response with the minimum amount of information possible. In order to  
 442 improve the resolution at these regions, the total number of clusters could be increased or, more wisely, a



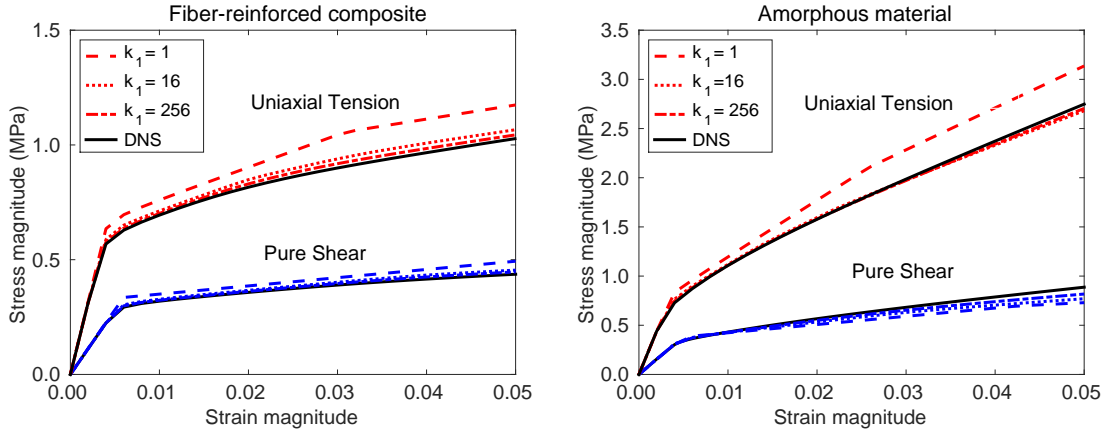


Figure 7: The predictions given by the proposed reduced order method with the self-consistent scheme for the fiber-reinforced composite (left) and amorphous material (right) under uniaxial tension and pure shear conditions. The solid lines represent the DNS results for comparison. Three different numbers of clusters in phase 1 were considered:  $k_1 = 1$  (dashes),  $k_1 = 16$  (dots) and  $k_1 = 256$  (dash-dots).

443 nonlinear mapping of the k-means clustering could be applied so that more clusters are assigned to regions  
 444 needing higher resolution (the issue is finding these regions, since different loading conditions lead to different  
 445 localization areas).

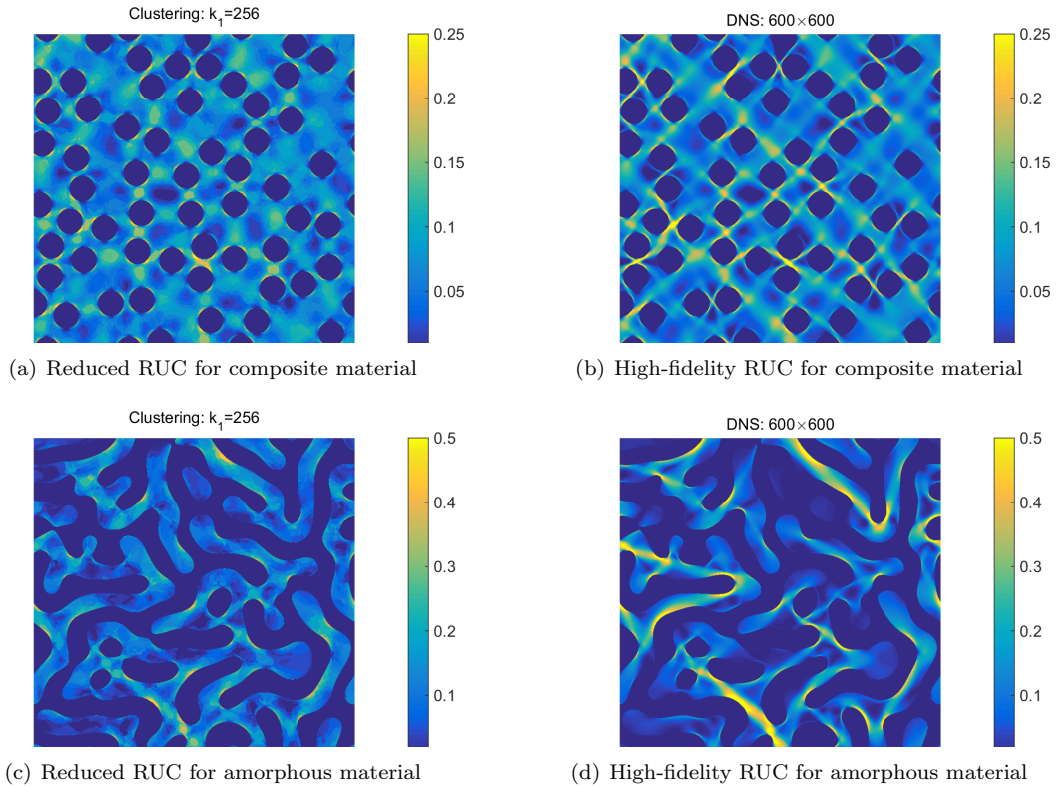


Figure 8: Equivalent plastic strain fields obtained from the direct numerical simulation of the high-fidelity RUC and from the self-consistent clustering analysis of the reduced RUC. Top row shows results for fiber-reinforced composite material, while bottom row presents the results for the amorphous material

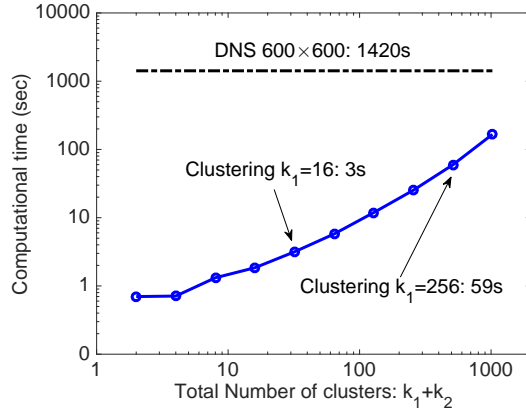


Figure 9: The computational time of the reduced order method with the self-consistent scheme vs. the total number of clusters  $k_1 + k_2$ . 25 incremental loading steps are considered. A typical DNS with mesh size  $600 \times 600$  takes 1420s.

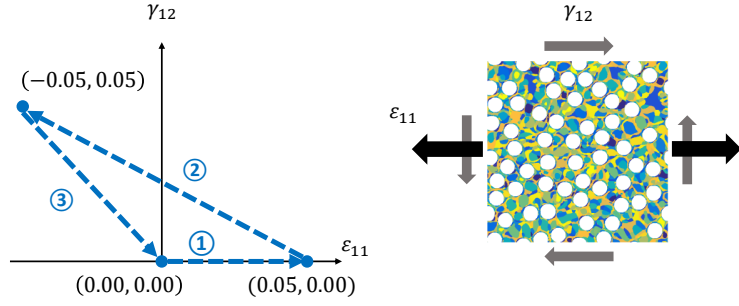
446 Up to this point the computational cost reduction of the method was not quantified. Even though the  
 447 reduction achieved in the number of degrees of freedom is obvious, the system of equations that is being solved  
 448 uses an iterative approach and each equation involves the summation over every cluster. Therefore, there is  
 449 a clear trade-off between the compression of information achieved by the clustering procedure and the actual  
 450 solution of the Lippmann-Schwinger equations. Figure 9 shows a comparison of computation time between  
 451 the proposed approach for different numbers of clusters and the DNS. The results are encouraging, especially  
 452 considering that the DNS finite element analyses were performed using a commercial code (significantly  
 453 optimized), while the proposed method was implemented in MATLAB. A typical two-dimensional DNS  
 454 took about 1420s ( $\approx 24$ min) on one intel i7-3632 processor, while the online stage of the reduced order  
 455 method with the self-consistent scheme (in MATLAB) took 4s for  $k_1 = 16$  and 75s for  $k_1 = 256$ . For  
 456  $k_1 \in [1, 512]$ , the computational time is almost proportional to the number of clusters in the system, which  
 457 indicates that the most time-consuming part is to update the internal variables locally at each cluster.

458 Finally, the reduced order model was also validated against a complex loading path. Macro-strain  
 459 constraints are applied on  $\varepsilon_{11}$  and  $\gamma_{12}$ , while  $\sigma_{22} = 0$ . Thus, the loading state can be represented by  
 460  $(\varepsilon_{11}, \gamma_{12})$ . As shown in Figure 10a), there are three steps in the loading path and the material finally returns  
 461 to the initial state ( $\varepsilon_{11} = 0, \gamma_{12} = 0$ ). Due to plasticity,  $\varepsilon_{22}$  does not necessarily vanish at the final state,  
 462 which means that the initial state with  $\varepsilon_{22} = 0$  is not reproduced. The stress-strain curves  $\sigma_{11}$ -vs- $\varepsilon_{11}$  and  
 463  $\sigma_{12}$ -vs- $\gamma_{12}$  given by the reduced-order method and the DNS results are shown in Figure 10 b) and c). Once  
 464 again good agreement is observed.

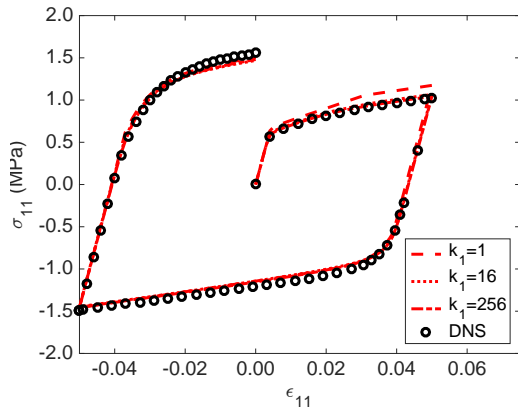
### 465 3.3. Three-dimensional nonlinear elasto-plastic material

466 The proposed method was also applied to 3D nonlinear elasto-plastic materials similar to the previously  
 467 presented examples in 2D. First, a spherical-particle composite is considered with the phase 1 being the  
 468 matrix (as before) and the number of matrix clusters being  $k_1$ . The volume fraction of the particle phase  
 469 (phase 2) was considered to be 20% and  $k_2 = \lceil k_1/4 \rceil$ . All the material properties are the same as before  
 470 (see equations (45), (46) and (47)). The mesh size of the finite element model considered as the DNS was  
 471  $64 \times 64 \times 64$ , and the illustration of the mesh in the inclusion phase (phase 2) is demonstrated in Figure  
 472 11. The reader is reminded that when generating the raw data, the strain concentration tensor  $\mathbf{A}(\mathbf{x})$  has  
 473 36 independent components since this is a 3D RUC. Thus, the dimension of data becomes 36, and a linear  
 474 increase in the running time of the k-means clustering occurs.

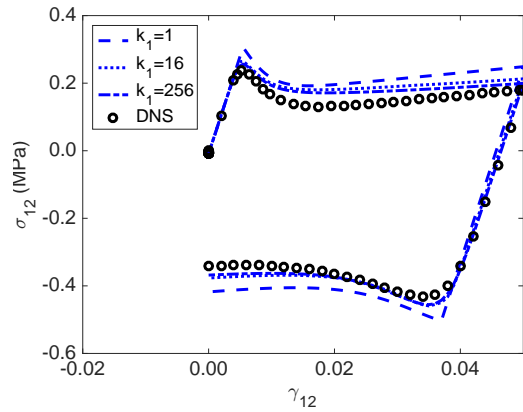
475 The stress-strain curves given by the self-consistent clustering analysis of the reduced RUC and the DNS  
 476 of the high-fidelity RUC results are plotted in Figure 11. Although the convergence rates of macroscopic  
 477 mechanical properties with respect to the number of clusters in 3D is not as high as the ones in 2D, good  
 478 accuracy can be achieved by assigning 256 clusters in phase 1 (320 in total) under both loading conditions.  
 479 In terms of computational cost, a typical DNS with  $64 \times 64 \times 64$  mesh took 7.3 hours on 24 cores (in a



(a) Illustrations of the complex loading path  $(\varepsilon_{11}, \gamma_{12})$ , where  $\varepsilon_{11}$  and  $\gamma_{12}$  are imposed as shown and  $\sigma_{22} = 0$



(b) Normal stress versus normal strain



(c) Shear stress versus shear strain

Figure 10: Response of the reduced RUC for the fiber-reinforced composite material under the three step loading path shown in (a):  $(0.00, 0.00) \rightarrow (0.05, 0.00) \rightarrow (-0.05, 0.05) \rightarrow (0.00, 0.00)$ . The  $\sigma_{11}$ -vs- $\varepsilon_{11}$  response is shown in (b), and the  $\sigma_{12}$ -vs- $\varepsilon_{12}$  response is presented in (c).

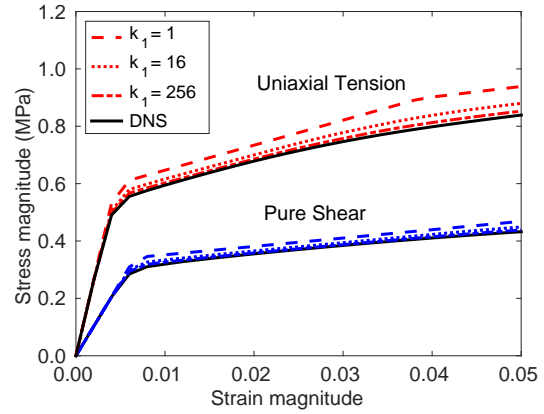
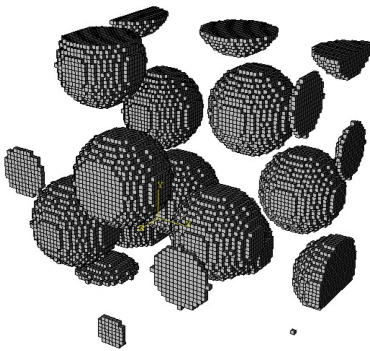


Figure 11: The  $64 \times 64 \times 64$  FE mesh of the 3D material displayed in the inclusion phase (phase 2) and stress-strain curves under uniaxial tension and pure shear loading conditions. The solid lines represent the DNS results for comparison. Three different numbers of clusters in phase 1 were considered:  $k_1 = 1$  (dashes),  $k_1 = 16$  (dots) and  $k_1 = 256$  (dash-dots).

480 state-of-the art high performance computing cluster with the following compute nodes: Intel Haswell E5-  
 481 2680v3 2.5GHz 12-cores). The reduced order method (in MATLAB) took 5s and 214s on one intel i7-3632

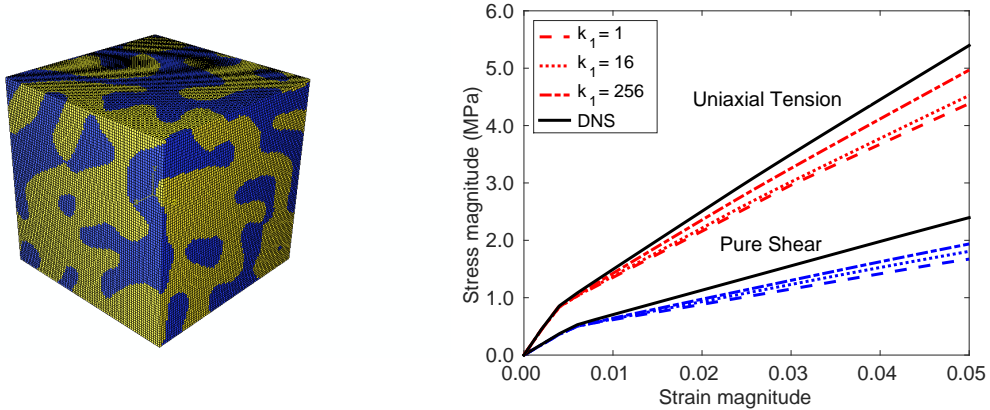


Figure 12: The  $80 \times 80 \times 80$  FE mesh of the 3D amorphous material and stress-strain curves under uniaxial tension and pure shear loading conditions. The solid lines represent the DNS results for comparison. Three different numbers of clusters in phase 1 were considered:  $k_1 = 1$  (dashes),  $k_1 = 16$  (dots) and  $k_1 = 256$  (dash-dots).

processor for  $k_1 = 16$  and  $k_1 = 256$ , respectively. A more refined finite element mesh was used for the same microstructure,  $80 \times 80 \times 80$ , and the differences in the stress-strain curves were less than 1% for both DNS and reduced order methods, indicating good convergence. For this case the DNS takes approximately 25.7 hours on the same 24 cores, while the reduced model computation time is the same (it only depends on the number of clusters).

The final example chosen to present in this work is a 3D two-phase amorphous material obtained by solving the Cahn-Hilliard equation in 3D. The illustration of the 3D microstructure is shown in Figure 12 and the finite element mesh considered for the DNS was  $80 \times 80 \times 80$ . The volume fraction of each phase was defined as 50%, so  $k_2 = k_1$  in the clustering step. The stress-strain curves in Figure 12 show that the predictions given by the reduced order method converge slower than all the previous examples considered: this is attributed to the complexity of microstructure in the 3D amorphous material that leads to fewer similarities in the local stress/strain field, implying the need to use more clusters in order to characterize the nonlinear behavior appropriately.

#### 4. Conclusion

A new computational approach was introduced for modeling the behavior of heterogeneous materials with complex microstructure. The proposed method includes two major contributions: 1) a data-compression procedure to improve the offline stage based on k-means clustering to group material subdomains with similar mechanical behavior; and 2) a new analysis method termed “self-consistent clustering analysis” derived via the homogeniation of each material subdomain (material cluster) through the Lippmann-Schwinger equation. The combination of the data compression achieved at the offline stage and the new scheme for solving the Lippmann-Schwinger equation *without* additional parameters or constitutive laws was shown to lead to a methodology with several attractive features: accurate, good convergence under refinement, computationally efficient, and involving a minimum amount of effort for both the offline and online stages. The offline stage is trivial since it only involves linear elastic simulations under 3 loading conditions for two-dimensional cases, or 6 loading conditions for three-dimensional ones.

As a final note, the proposed method is believed to have a wide range of applications to various material systems. Multifunctional and multiphysics material systems such as piezoelectric and thermomechanical materials may be interesting future applications. The particular case of nonlinear materials with strain softening or damage requires special attention, since the effective modulus becomes negative in the softening region and the current fix-point method for solving the self-consistent reference material needs to be modified

512 to improve convergence. A possible way is to work with the total form of the Lippmann-Schwinger equation  
 513 instead of the incremental form, i.e. with  $\boldsymbol{\sigma}(\mathbf{x})$  and  $\boldsymbol{\varepsilon}(\mathbf{x})$  as variables.

## 514 Acknowledgement

515 Z.L., M.A.B and W.K.L. warmly thank the support from AFOSR grant No. FA9550-14-1-0032. Z.L.  
 516 would like to thank Prof. Wei Chen and Stephen Lin for their parts in helpful discussions. M.A.B. would  
 517 like to acknowledge support from the Portuguese National Science Foundation and the Fulbright Program,  
 518 and to thank Prof. Jacob Fish and Dr. Brendan Abberton for their parts in helpful discussions.

## 519 Appendix A. Calculation and clustering of $\mathbf{A}$

520 In order to generate the database with the strain concentration tensors  $\mathbf{A}(\mathbf{x})$ , we implemented the DNS  
 521 method based on fast Fourier transforms [19], which iteratively solves the full Lippmann-Schwinger equation  
 522 with periodic boundary conditions. The finite element method could also be used to calculate  $\mathbf{A}(\mathbf{x})$ . As  
 523 mentioned in Section 2.2.1, three orthogonal loading conditions are needed for a 2D material. In Voigt  
 524 notation  $\{\boldsymbol{\varepsilon}^{\text{macro}}\} = [\varepsilon_{11}^{\text{macro}}, \varepsilon_{22}^{\text{macro}}, \gamma_{12}^{\text{macro}}]$ , the loading conditions in terms of the macroscopic strain are  
 525 listed as  $[1, 0, 0]$ ,  $[0, 1, 0]$  and  $[0, 0, 1]$ . For instance, component  $A_{11}$ ,  $A_{21}$  and  $A_{31}$  are obtained under condition  
 526  $\{\boldsymbol{\varepsilon}^{\text{macro}}\} = [1, 0, 0]$ .

527 In this paper, we use the standard algorithm (Lloyd's algorithm) [48] to solve the k-means clustering  
 528 problem. The standard algorithm is essentially an optimization process of minimizing the within-cluster  
 529 least squares sum,

$$\mathbf{S} = \underset{\mathbf{S}'}{\operatorname{argmin}} \sum_{J=1}^k \sum_{n \in S^J} \|\mathbf{A}_n - \bar{\mathbf{A}}_J\|^2, \quad (\text{A.1})$$

530 where  $\mathbf{A}_n$  is the strain concentration tensor of the  $n$ -th data point in Voigt notation, and  $\bar{\mathbf{A}}_J$  is the mean  
 531 of all the strain concentration tensors at the points within the cluster  $S_J$ .

532 At the initialization step,  $k$  data points are randomly selected from the data set and served as the initial  
 533 means (Forgy method [55]). Then the algorithm iterates between the following two steps,

- 534 1. Assignment step: Each data point is assigned to the cluster whose mean is nearest to the data point.  
 535 In other words, within the  $t$ -th iteration,  $\forall \{\mathbf{A}_n\} \in S_I^{(t)}$ , we have

$$\|\{\mathbf{A}_n\} - \bar{\mathbf{A}}_I^{(t)}\|^2 \leq \|\{\mathbf{A}_n\} - \bar{\mathbf{A}}_J^{(t)}\|^2 \quad \forall J, J \neq I \quad (\text{A.2})$$

- 536 2. Update step: The mean values of the data points in the new cluster are recalculated for iteration  $t+1$ ,

$$\bar{\mathbf{A}}_I^{(t)} = \frac{1}{N_I^{(t)}} \sum_{\{\mathbf{A}_n\} \in S_I^{(t)}} \{\mathbf{A}_n\} \quad (\text{A.3})$$

538 where  $N_i^{(t)}$  is the number of data points in cluster  $S_I^{(t)}$ .

539 When the assignment of data points no longer changes, the algorithm is said to converge to a local optimum.  
 540 However, the global optimum is not guaranteed in the optimization process. Therefore, k-means clustering  
 541 is always performed with multiple replications in real application in order to overcome the local barrier.

## 542 Appendix B. Different elastic properties in the online stage without redoing the offline stage

543 The proposed approach predicts new effective elastic properties of the RUC when considering new elastic  
 544 properties for each phase of the material with the same microstructure, even when considering the same  
 545 selection of elastic properties in the offline stage, equation (45).

546 Several simulations in the online stage were conducted using different Young's modulus of phase 2 ( $E_2$   
547 was varied from 1 to 5000MPa), while keeping the Young's modulus of phase 1 at 100 MPa. The Young's  
548 moduli ratio between phase 2 and phase 1 ranged from 0.01 to 50. The DNS results obtained for this range  
549 are provided in Figure B.13, where the microstructural effect on the overall material behavior is clear. Note  
550 that since phase 2 in the fiber-reinforced composite is discontinuous (fibers are separated), the effect of  
551 varying its modulus  $E_2$  is less pronounced and the overall properties are mainly determined by the matrix  
552 material. On the other hand, the overall modulus keeps increasing with  $E_2$  in the amorphous material,  
553 where phases 1 and 2 are irregular and similar to each other.

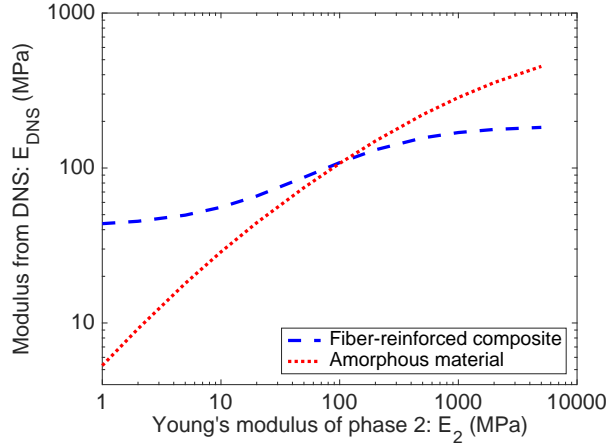


Figure B.13: Equivalent transverse Young modulus  $E_{\text{DNS}}$  of the RUC obtained from DNS as a function of the Young's modulus of phase 2.

554 Figure B.14 shows the results from the proposed method with and without the self-consistent scheme.  
555 Once again the improvement from the self-consistent scheme is evident, where the transverse Young's modu-  
556 lus is close to the DNS values for a significant range of ratios (0.01 – 50). Without the self-consistent scheme,  
557 especially for the amorphous material, there is a tendency to overestimate or underestimate the modulus at  
558 extreme cases even using a large number of clusters, indicating that phase 1 is no longer a good candidate  
559 for the reference material.

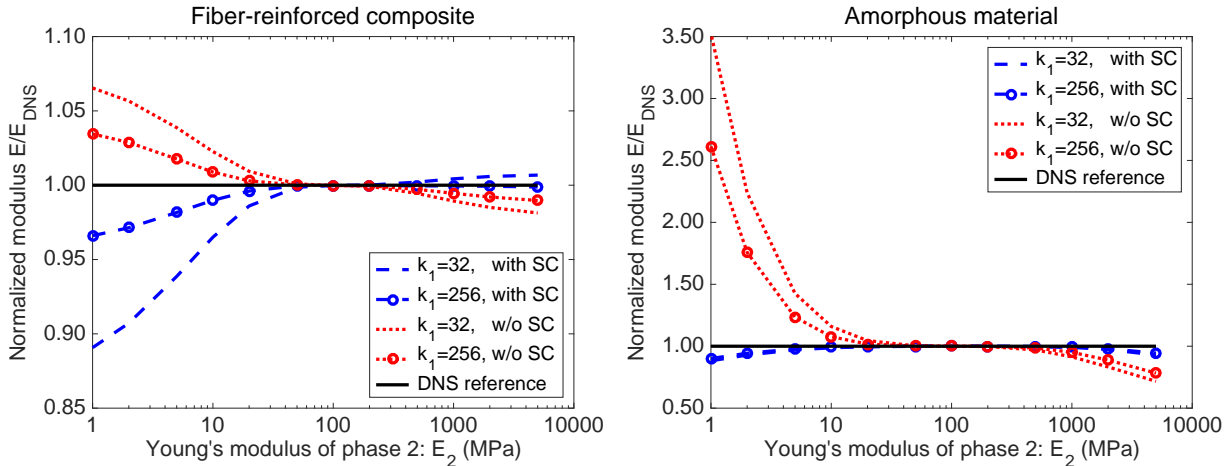


Figure B.14: The effects of phase 2 Young's modulus  $E_2$  on the overall normalized equivalent transverse Young's modulus for the fiber-reinforced material (left) and amorphous material (right). Results from  $k_1 = 32$  and 256 are provided with and without the self-consistent scheme (SC).

560 These results demonstrate that reasonable elastic predictions are possible even without going through

561 the offline process for new combinations of elastic properties. Nevertheless, in practice the offline stage of  
562 the proposed method is so simple (three loading conditions in 2D, and six in 3D) that avoiding it is usually  
563 not worthwhile.

## 564 References

- 565 [1] A. L. Gurson, Continuum theory of ductile rupture by void nucleation and growth: Part i yield criteria and flow rules for  
566 porous ductile media, *Journal of engineering materials and technology* 99 (1) (1977) 2–15.
- 567 [2] E. de Souza Neto, D. Peric, D. Owen, *Computational methods for plasticity: theory and applications*, Wiley, 2008.
- 568 [3] P. Camanho, M. Bessa, G. Catalanotti, M. Vogler, R. Rolfes, Modeling the inelastic deformation and fracture of polymer  
569 composites part ii: Smeared crack model, *Mechanics of Materials* 59 (0) (2013) 36 – 49.
- 570 [4] F. Feyel, J.-L. Chaboche, Fe 2 multiscale approach for modelling the elastoviscoplastic behaviour of long fibre sic/ti  
571 composite materials, *Computer methods in applied mechanics and engineering* 183 (3) (2000) 309–330.
- 572 [5] V. Kouznetsova, M. G. D. Geers, W. A. M. Brekelmans, Multi-scale constitutive modelling of heterogeneous materials with  
573 a gradient-enhanced computational homogenization scheme, *International Journal for Numerical Methods in Engineering*  
574 54 (8) (2002) 1235–1260.
- 575 [6] F. Feyel, A multilevel finite element method (fe2) to describe the response of highly non-linear structures using generalized  
576 continua, *Computer Methods in Applied Mechanics and Engineering* 192 (2830) (2003) 3233 – 3244, *Multi-scale  
577 Computational Mechanics for Materials and Structures*.
- 578 [7] G. J. Wagner, W. K. Liu, Coupling of atomistic and continuum simulations using a bridging scale decomposition, *Journal  
579 of Computational Physics* 190 (1) (2003) 249 – 274.
- 580 [8] H. Kadowaki, W. K. Liu, Bridging multi-scale method for localization problems, *Computer Methods in Applied Mechanics  
581 and Engineering* 193 (3032) (2004) 3267 – 3302, *computational Failure Mechanics*.
- 582 [9] H. Kadowaki, W. K. Liu, A multiscale approach for the micropolar continuum model, *Computer Modeling in Engineering  
583 and Sciences* 7 (3) (2005) 269–282.
- 584 [10] H. S. Park, E. G. Karpov, P. A. Klein, W. K. Liu, Three-dimensional bridging scale analysis of dynamic fracture, *Journal  
585 of Computational Physics* 207 (2) (2005) 588 – 609.
- 586 [11] S. Tang, T. Y. Hou, W. K. Liu, A pseudo-spectral multiscale method: Interfacial conditions and coarse grid equations,  
587 *Journal of Computational Physics* 213 (1) (2006) 57 – 85.
- 588 [12] X. Bai, M. Bessa, A. Melro, P. Camanho, L. Guo, W. Liu, High-fidelity micro-scale modeling of the thermo-visco-plastic  
589 behavior of carbon fiber polymer matrix composites, *Composite Structures* (2015) –.
- 590 [13] N. Vu-Bac, M. Bessa, T. Rabczuk, W. Liu, A multiscale model for the quasi-static thermo-plastic behavior of highly  
591 cross-linked glassy polymers, Submitted to publication.
- 592 [14] J. D. Eshelby, The determination of the elastic field of an ellipsoidal inclusion, and related problems, in: *Proceedings of  
593 the Royal Society of London A: Mathematical, Physical and Engineering Sciences*, Vol. 241, The Royal Society, 1957, pp.  
594 376–396.
- 595 [15] Z. Hashin, S. Shtrikman, A variational approach to the theory of the elastic behaviour of multiphase materials, *Journal  
596 of the Mechanics and Physics of Solids* 11 (2) (1963) 127–140.
- 597 [16] R. Hill, A self-consistent mechanics of composite materials, *Journal of the Mechanics and Physics of Solids* 13 (4) (1965)  
598 213–222.
- 599 [17] Z. Liu, J. A. Moore, S. M. Aldousari, H. S. Hedia, S. A. Asiri, W. K. Liu, A statistical descriptor based volume-integral  
600 micromechanics model of heterogeneous material with arbitrary inclusion shape, *Computational Mechanics* (2015) 1–19.
- 601 [18] S. Ghosh, K. Lee, S. Moorthy, Two scale analysis of heterogeneous elastic-plastic materials with asymptotic homogenization  
602 and voronoi cell finite element model, *Computer Methods in Applied Mechanics and Engineering* 132 (12) (1996) 63 –  
603 116.
- 604 [19] H. Moulinec, P. Suquet, A numerical method for computing the overall response of nonlinear composites with complex  
605 microstructure, *Computer Methods in Applied Mechanics and Engineering* 157 (12) (1998) 69 – 94.
- 606 [20] J. Aboudi, A continuum theory for fiber-reinforced elastic-viscoplastic composites, *International Journal of Engineering  
607 Science* 20 (5) (1982) 605–621.
- 608 [21] M. Paley, J. Aboudi, Micromechanical analysis of composites by the generalized cells model, *Mechanics of Materials* 14 (2)  
609 (1992) 127–139.
- 610 [22] G. J. Dvorak, Transformation field analysis of inelastic composite materials 437 (1900) (1992) 311–327.
- 611 [23] J. Michel, P. Suquet, Nonuniform transformation field analysis, *International Journal of Solids and Structures* 40 (25)  
612 (2003) 6937 – 6955, special issue in Honor of George J. Dvorak.
- 613 [24] S. Roussette, J.-C. Michel, P. Suquet, Nonuniform transformation field analysis of elastic–viscoplastic composites, *Com-  
614 posites Science and Technology* 69 (1) (2009) 22–27.
- 615 [25] K. Karhunen, *Zur spektraltheorie stochastischer prozesse*, *Suomalainen tiedeakatemia*, 1946.
- 616 [26] M. Loève, *Probability Theory; Foundations, Random Sequences*, New York: D. Van Nostrand Company, 1955.
- 617 [27] I. Jolliffe, *Principal component analysis*, Wiley Online Library, 2002.
- 618 [28] G. Berkooz, P. Holmes, J. L. Lumley, The proper orthogonal decomposition in the analysis of turbulent flows, *Annual  
619 review of fluid mechanics* 25 (1) (1993) 539–575.
- 620 [29] J. Yvonnet, Q.-C. He, The reduced model multiscale method (r3m) for the non-linear homogenization of hyperelastic  
621 media at finite strains, *Journal of Computational Physics* 223 (1) (2007) 341–368.

- 622 [30] O. Goury, D. Amsallem, S. P. A. Bordas, W. K. Liu, P. Kerfriden, Automatised selection of load paths to construct  
623 reduced-order models in computational damage micromechanics: from dissipation-driven random selection to bayesian  
624 optimisation, *Computational Mechanics*.
- 625 [31] D. Néron, P.-A. Boucard, N. Relun, Time-space pgd for the rapid solution of 3d nonlinear parametrized problems in the  
626 many-query context, *International Journal for Numerical Methods in Engineering* 103 (4) (2015) 275–292.
- 627 [32] P. Ladevèze, *Nonlinear computational structural mechanics: new approaches and non-incremental methods of calculation*,  
628 Springer Science & Business Media, 2012.
- 629 [33] A. Ammar, B. Mokdad, F. Chinesta, R. Keunings, A new family of solvers for some classes of multidimensional partial  
630 differential equations encountered in kinetic theory modeling of complex fluids, *Journal of Non-Newtonian Fluid Mechanics*  
631 139 (3) (2006) 153 – 176.
- 632 [34] P. Ladevèze, J.-C. Passieux, D. Néron, The {LATIN} multiscale computational method and the proper generalized de-  
633 composition, *Computer Methods in Applied Mechanics and Engineering* 199 (2122) (2010) 1287 – 1296, *Multiscale Models*  
634 *and Mathematical Aspects in Solid and Fluid Mechanics*.
- 635 [35] F. Chinesta, A. Ammar, A. Leygue, R. Keunings, An overview of the proper generalized decomposition with applications  
636 in computational rheology, *Journal of Non-Newtonian Fluid Mechanics* 166 (11) (2011) 578 – 592.
- 637 [36] C. Ghatas, F. Masson, A. Huerta, A. Leygue, E. Cueto, F. Chinesta, Proper generalized decomposition based dynamic  
638 data-driven control of thermal processes, *Computer Methods in Applied Mechanics and Engineering* 213216 (2012) 29 –  
639 41.
- 640 [37] P. Kerfriden, O. Goury, T. Rabczuk, S. P.-A. Bordas, A partitioned model order reduction approach to rationalise  
641 computational expenses in nonlinear fracture mechanics, *Computer methods in applied mechanics and engineering* 256  
642 (2013) 169–188.
- 643 [38] C. Oskay, J. Fish, Eigendeformation-based reduced order homogenization for failure analysis of heterogeneous materials,  
644 *Computer Methods in Applied Mechanics and Engineering* 196 (7) (2007) 1216 – 1243.
- 645 [39] J. Chaboche, P. Kanout, A. Roos, On the capabilities of mean-field approaches for the description of plasticity in metal  
646 matrix composites, *International Journal of Plasticity* 21 (7) (2005) 1409 – 1434.
- 647 [40] J. Fish, *Practical multiscale modeling*, John Wiley & Sons, 2013.
- 648 [41] F. Fritzen, M. Leuschner, Reduced basis hybrid computational homogenization based on a mixed incremental formulation,  
649 *Computer Methods in Applied Mechanics and Engineering* 260 (2013) 143–154.
- 650 [42] Z. Hashin, S. Shtrikman, A variational approach to the theory of the elastic behaviour of polycrystals, *Journal of the*  
651 *Mechanics and Physics of Solids* 10 (4) (1962) 343–352.
- 652 [43] J. MacQueen, et al., Some methods for classification and analysis of multivariate observations, in: *Proceedings of the fifth*  
653 *Berkeley symposium on mathematical statistics and probability*, Vol. 1, Oakland, CA, USA., 1967, pp. 281–297.
- 654 [44] J. W. Cahn, J. E. Hilliard, Free energy of a nonuniform system. i. interfacial free energy, *The Journal of chemical physics*  
655 28 (2) (1958) 258–267.
- 656 [45] L. Barghout, J. Sheynin, Real-world scene perception and perceptual organization: Lessons from computer vision, *Journal*  
657 *of Vision* 13 (9) (2013) 709–709.
- 658 [46] W. Li, L. Jaroszewski, A. Godzik, Clustering of highly homologous sequences to reduce the size of large protein databases,  
659 *Bioinformatics* 17 (3) (2001) 282–283.
- 660 [47] I. H. Witten, E. Frank, *Data Mining: Practical machine learning tools and techniques*, Morgan Kaufmann, 2005.
- 661 [48] S. P. Lloyd, Least squares quantization in pcm, *Information Theory, IEEE Transactions on* 28 (2) (1982) 129–137.
- 662 [49] T. Kanungo, D. M. Mount, N. S. Netanyahu, C. D. Piatko, R. Silverman, A. Y. Wu, An efficient k-means clustering  
663 algorithm: Analysis and implementation, *Pattern Analysis and Machine Intelligence, IEEE Transactions on* 24 (7) (2002)  
664 881–892.
- 665 [50] P. J. Rousseeuw, Silhouettes: a graphical aid to the interpretation and validation of cluster analysis, *Journal of computa-*  
666 *tional and applied mathematics* 20 (1987) 53–65.
- 667 [51] J. C. Michel, H. Moulinec, P. Suquet, A computational scheme for linear and non-linear composites with arbitrary phase  
668 contrast, *International Journal for Numerical Methods in Engineering* 52 (1-2) (2001) 139–160.
- 669 [52] V. Monchiet, G. Bonnet, A polarization-based fft iterative scheme for computing the effective properties of elastic com-  
670 posites with arbitrary contrast, *International Journal for Numerical Methods in Engineering* 89 (11) (2012) 1419–1436.
- 671 [53] J. Yvonnet, A fast method for solving microstructural problems defined by digital images: a space lippmann–schwinger  
672 scheme, *International Journal for Numerical Methods in Engineering* 92 (2) (2012) 178–205.
- 673 [54] C. M. Breneman, L. C. Brinson, L. S. Schadler, B. Natarajan, M. Krein, K. Wu, L. Morkowchuk, Y. Li, H. Deng, H. Xu,  
674 *Stalking the materials genome: A data-driven approach to the virtual design of nanostructured polymers*, *Advanced*  
675 *Functional Materials* 23 (46) (2013) 5746–5752.
- 676 [55] E. W. Forgy, Cluster analysis of multivariate data: efficiency versus interpretability of classifications, *Biometrics* 21 (1965)  
677 768–769.